AMERICAN SOCIETY FOR MICROBIOLOGY | Journal of Virology®

Channel-Inactivating Mutations and Their Revertant Mutants in the Envelope Protein of Infectious Bronchitis Virus

Janet To,[a] Wahyu Surya,[a] To Sing Fung,[a] Yan Li,[a] Carmina Verdià-Bàguena,[b] Maria Queralt-Martin,[b] Vicente M. Aguilella,[b] Ding Xiang Liu,[a] Jaume Torres[a]

School of Biological Sciences, Nanyang Technological University, Singapore, Singapore[a]; Department of Physics, Laboratory of Molecular Biophysics. Universitat Jaume I, Castelló, Spain[b]

ABSTRACT It has been shown previously in the severe acute respiratory syndrome coronavirus (SARS-CoV) that two point mutations, N15A and V25F, in the transmembrane domain (TMD) of the envelope (E) protein abolished channel activity and led to *in vivo* attenuation. Pathogenicity was recovered in mutants that also regained E protein channel activity. In particular, V25F was rapidly compensated by changes at multiple V25F-facing TMD residues located on a neighboring monomer, consistent with a recovery of oligomerization. Here, we show using infected cells that the same mutations, T16A and A26F, in the gamma-CoV infectious bronchitis virus (IBV) lead to, in principle, similar results. However, IBV E A26F did not abolish oligomer formation and was compensated by mutations at N- and C-terminal extramembrane domains (EMDs). The C-terminal EMD mutations clustered along an insertion sequence specific to gamma-CoVs. Nuclear magnetic resonance data are consistent with the presence of only one TMD in IBV E, suggesting that recovery of channel activity and fitness in these IBV E revertant mutants is through an allosteric interaction between EMDs and TMD. The present results are important for the development of IBV live attenuated vaccines when channel-inactivating mutations are introduced in the E protein.

IMPORTANCE The ion channel activity of SARS-CoV E protein is a determinant of virulence, and abolishment of channel activity leads to viral attenuation. E deletion may be a strategy for generating live attenuated vaccines but can trigger undesirable compensatory mechanisms through modifications of other viral proteins to regain virulence. Therefore, a more suitable approach may be to introduce small but critical attenuating mutations. For this, the stability of attenuating mutations should be examined to understand the mechanisms of reversion. Here, we show that channel-inactivating mutations of the avian infectious bronchitis virus E protein introduced in a recombinant virus system are deficient in viral release and fitness and that revertant mutations also restored channel activity. Unexpectedly, most of the revertant mutations appeared at extramembrane domains, particularly along an insertion specific for gammacoronaviruses. Our structural data propose a single transmembrane domain in IBV E, suggesting an allosteric interaction between extramembrane and transmembrane domains.

KEYWORDS coronavirus, infectious bronchitis virus, envelope protein, channel activity, NMR structure, small membrane protein

Received 1 November 2016 **Accepted** 6 December 2016

Accepted manuscript posted online 14 December 2016

Citation To J, Surya W, Fung TS, Li Y, Verdià-Bàguena C, Queralt-Martin M, Aguilella VM, Liu DX, Torres J. 2017. Channel-inactivating mutations and their revertant mutants in the envelope protein of infectious bronchitis virus. J Virol 91:e02158-16. https://doi.org/10.1128/JVI.02158-16.

Editor Stanley Perlman, University of Iowa

Address correspondence to Ding Xiang Liu, dxliu0001@163.com, or Jaume Torres, jtorres@ntu.edu.sg.

J. To, W. Surya, and T. S. Fung contributed equally to this article.

The avian infectious bronchitis virus (IBV) is a coronavirus (CoV) first isolated in 1937 (1) that can seriously devastate and cause severe economic losses to the poultry industry worldwide (2). IBV is highly contagious and causes pathology ranging from mild respiratory symptoms to severe kidney and oviduct diseases, which translates into poor weight gain, renal disease, and decreased egg production and quality. It has been

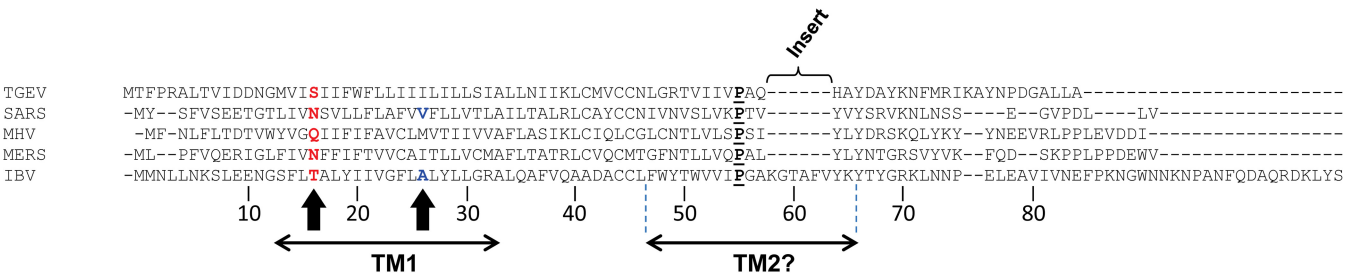

FIG 1 Sequence alignment of representative CoV E proteins. Amino acid sequence of E proteins from TGEV (transmissible gastroenteritis virus; NCBI accession no. ABG89336.1) (alpha-CoV), MHV (murine hepatitis virus; AAC36596.1), SARS-CoV (severe acute respiratory syndrome coronavirus; NP_828854.1), Middle-East respiratory syndrome coronavirus (MERS-CoV; YP_009047209.1) (beta-CoV), and IBV (infectious bronchitis virus; P05139.2) (gamma-CoV). The alignment was obtained using Clustal O (https://www.ebi.ac.uk/Tools/msa/clustalo/) and shows an "insert" sequence specific to IBV E. The positions previously mutated in SARS-CoV E that generated IC-inactive mutants (32) are indicated with vertical arrows, with the first arrow pointing to conserved polar residues (red). Numbering corresponds to the IBV E sequence. Two putative TMDs are indicated, predicted with TMHMM 2.0 (http://www.cbs.dtu.dk/services/TMHMM-2.0/) (71) from residue 13 to 32 and from residue 47 to 65, although Phobius (http://phobius.sbc.su.se/) (47) predicts one TMD, from residue 12 to 31. The consensus secondary structure in the region represented by TM2 is predicted to have β-structure flanking a disordered coil around the conserved proline (NPS@: Network Protein Sequence Analysis [72]). In IBV E, this β-coil–β-region is represented by residues 48 to 68. A similar consensus secondary structure is predicted for E proteins in other CoVs, except alpha-CoVs (TGEV).

estimated that IBV infection in a commercial flock with the best possible management practice reduces income by approximately 3% (3).

CoVs are single-stranded positive-sense enveloped RNA viruses that belong to the subfamily *Coronavirinae* in the family *Coronaviridae* and are organized into four genera (4–6), namely, alpha-, beta-, gamma-, and delta-CoV. In humans, CoVs cause approximately 30% of common colds, whereas the severe acute respiratory syndrome coronavirus (SARS-CoV) and the recently emerged Middle East respiratory syndrome coronavirus (MERS-CoV) have produced near pandemics (7, 8).

No effective licensed treatments exist against coronavirus infections (9–11), but live attenuated vaccines (LAVs) (12–16) and fusion inhibitors (17) are promising strategies. Nevertheless, the chances of reappearance of virulent phenotypes, drug side effects, and resistance call for continued antiviral development, which depends on an intimate knowledge of the coronavirus molecular biology (18).

One CoV component critical for pathogenesis is the envelope (E) protein. E proteins are short polypeptides (76 to 109 amino acids) with at least one transmembrane domain (TMD) that exist in small amounts in virions but are found abundantly in internal membranes of infected cells, mostly localized to the endoplasmic reticulum-Golgi intermediate compartment (ERGIC) (19–24). In animal models, deletion of SARS-CoV E protein reduced pathogenicity and mortality (25), and a recombinant SARS-CoV lacking the E gene led to increased apoptosis and downregulation of genes related to inflammation in infected cells, whereas administration of E protein in *trans* reduced the stress response (26).

Development of CoV LAVs that are based on modifications of the E protein requires an accurate knowledge of critical residues and/or domains, as well as the compensatory mechanisms available to recover virulence. Deletion of E protein, as shown for SARS-CoV E, triggers unwanted compensation mechanisms that recover critical protein-protein interactions. For example, SARS-CoV ΔE passaged in cell culture led to the appearance of a chimeric membrane (M) gene; the last four amino acids of this chimeric protein formed PDZ-binding motifs (PBM) (27), shown to be critical for viral pathogenesis (28). Similarly, in mouse models, SARS-CoV ΔE led to the appearance of a mutated variant of 8a protein with an internal PBM which resulted in reversion to virulence (27). An alternative strategy may be to make small multiple but critical attenuating alterations, in a context where the functional domains of the protein are left almost intact, so as to improve the overall stability of the attenuated virus for the purpose of vaccine development.

CoV E proteins form homopentameric ion channels (IC) with poor or no ion selectivity (29, 30). Mutations at two residues in the predicted TMD of SARS-CoV E, N15A and V25F (Fig. 1), abolished channel activity *in vitro* (31). Compared with the wild-type

virus, these mutants displayed similar growth kinetics but reduced fitness in infected cells (32). However, introduction of these mutations in a recombinant mouse-adapted SARS-CoV (MA15) resulted in *in vivo* attenuation, and revertant mutants that regained viral fitness and pathogenicity also regained channel activity (32).

The TMD of SARS-CoV E has been characterized in lipid membranes (33, 34) and in dodecylphosphatidylcholine (DPC) micelles (35). Whereas Asn15 is facing the lumen of the channel, Val25 is close to the helix-helix interface (34, 35), although in another computational model, it was right at the helix-helix interface (33, 36). Consistent with the expectation that mutation V25F would disrupt TM-TM interactions, compensatory mutations clustered along the helix interface opposite Val25 (32).

Most outstanding, however, is that recombinant virus carrying mutation N15A in its E protein, which enabled mice to survive, did not revert to a more pathogenic phenotype *in vivo* (32). Only when multiple passages were performed in cell culture did the mutation A15D appear (and IC activity was regained). This is surprising because mutation A15D involves at least one transversion (C↔A), i.e., a conversion between purine and pyrimidine. Mutations to other polar residues were not selected by the virus (32) even when only a single transition was required, such as G↔A in A15T. Transitions are more likely than transversions, as they involve exchanges between two purines or between two pyrimidines (37).

From an alignment of E sequences representative of CoV groups, the position represented by Asn15 in SARS-CoV E is always occupied by a polar residue, Thr in gamma-CoV. IBV E mutation T16A resulted in decreased Golgi complex disruption (38, 39), proposed to facilitate the efficient trafficking of virions (38–42). However, the effects observed for T16A could not be restored by the conservative polar substitutions to Ser, Asn, or Gln (39). Since the IC activities of these IBV E mutants were not measured (32, 39), these effects cannot be unequivocally attributed to loss of IC activity. Nevertheless, these results suggest that CoV E proteins have an exquisite specificity for the identity of the polar residue at this position. Similarly, SARS-CoV E Val25 is aligned with IBV E Ala26, and therefore a similar pattern of revertant mutants would be expected for IBV E mutation A26F.

The latter hypothesis assumes that IBV E and SARS-CoV E adopt similar structures. However, although in general CoV E proteins have a cytoplasmic C-terminal domain and a lumenal N terminus (22, 24, 39, 43), the presence of a single α-helical TMD has been shown only for the E proteins of beta-CoVs SARS-CoV (33–36, 44, 45) and MERS-CoV (46). It is not known if additional TMDs or embedded motifs exist in other CoV E proteins. For example, two TMDs (residues 13 to 32 and 47 to 65) are predicted for IBV E using TMHMM (http://www.cbs.dtu.dk/services/TMHMM-2.0/), but only one TMD (residues 12 to 31) is predicted using Phobius (http://phobius.sbc.su.se/) (47).

Therefore, in the present study, we have generated recombinant IBVs (rIBV) harboring the above-mentioned mutations (T16A or A26F) in the E gene (rT16A and rA26F mutants) to test their effect on genome replication/transcription kinetics, protein translation, and virus assembly in the context of IBV infection in cells. We have also analyzed the revertant mutations that appear in the IBV E sequence and correlate their locations with structural features of IBV E obtained by solution nuclear magnetic resonance (NMR).

RESULTS

IBV E protein IC activity is not essential for virus replication in cell culture. Previous studies on SARS-CoV E showed that two residues in the TMD, Asn15 and Val25 (Fig. 1, arrows), are essential for IC activity, viral fitness, and pathogenesis (32). Based on the CoV E protein alignment, the two equivalent positions in IBV E are Thr16 and Ala26. Therefore, we hypothesized that similar mutations in IBV E protein, T16A and A26F, would also disrupt IC activity. To verify this, full-length IBV E proteins carrying each of these two mutations were expressed and purified, and channel activity was tested in black lipid membranes (BLM), i.e., supported lipid bilayers. While the wild-type IBV E

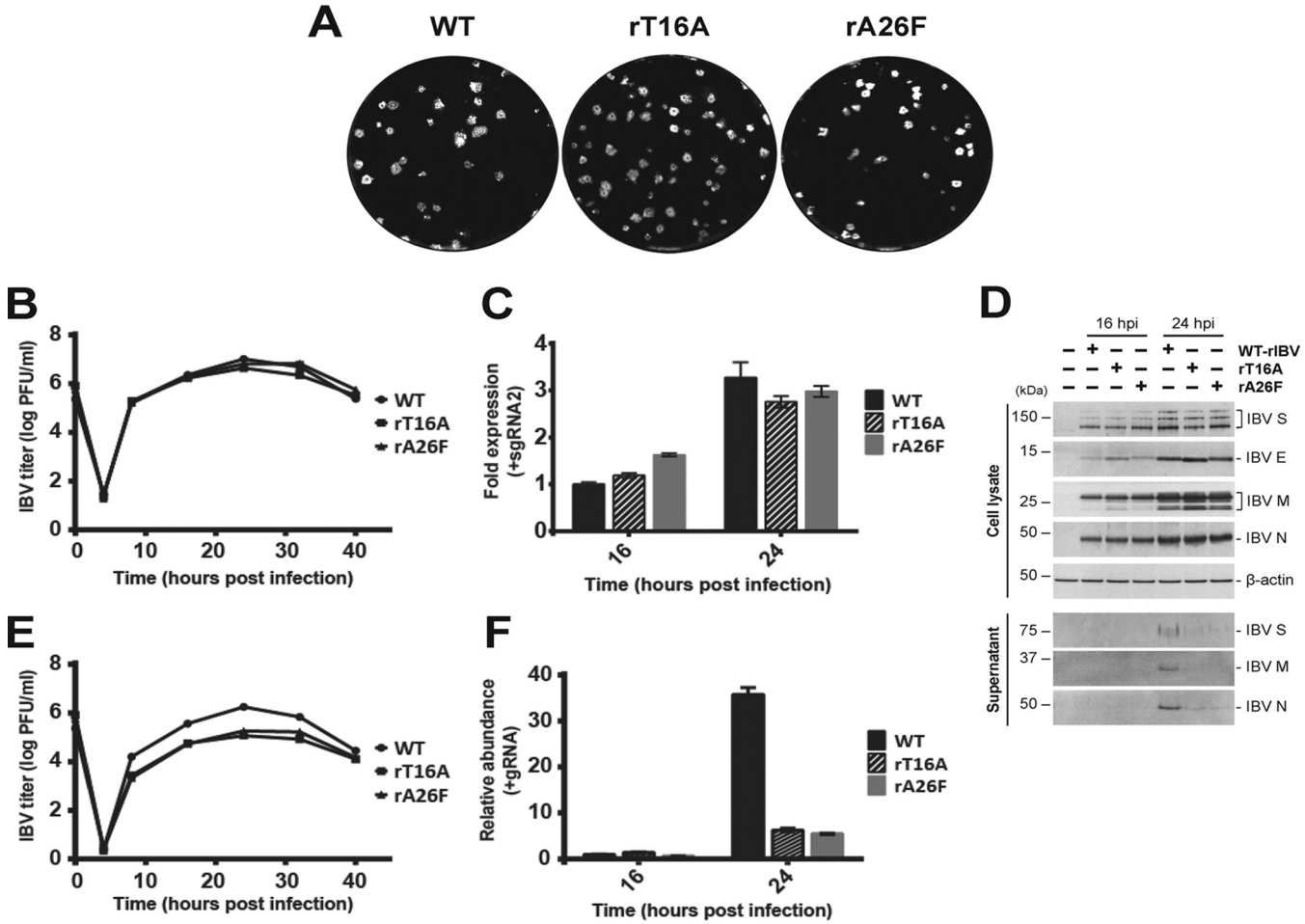

FIG 2 Growth properties of WT-rIBV and rT16A and rA26F mutant viruses. (A) Comparison of plaque morphologies of WT-rIBV and rT16A and rA26F mutant viruses. Plaque sizes: 1.00 ± 0.65 mm for WT, 0.88 ± 0.54 mm for rT16A mutant, and 0.59 ± 0.32 mm for rA26F mutant. (B) Vero cells were infected at an MOI of 2 with WT-rIBV, rT16A mutant, or rA26F mutant, and the viral progeny in total cell lysate was titrated at the indicated times postinfection. (C) Total cellular RNA was harvested from infected cells at the indicated times postinfection, and IBV positive-sense subgenomic RNA2 (+sgRNA2) levels were quantified by qPCR and normalized to an internal GAPDH control. (D) Western blot analysis of viral protein expression in Vero cells infected with the WT-rIBV, rT16A mutant, or rA26F mutant, harvested at the indicated time points. (E) Vero cells were infected as described for panel B, and viral progeny in culture supernatant was titrated. (F) RNA was extracted from culture supernatant of infected cells, and IBV positive-sense genomic RNA (+gRNA) levels were quantified relative to that of the wild type at 16 hpi. Error bars represent ±SEM.

showed channel activity, no conductance could be measured for either of these two mutants (not shown).

To investigate the impact of the loss of IBV E IC activity in the T16A and A26F mutants on IBV replication, these mutations were introduced in a recombinant IBV (rIBV), to obtain rIBV-E-T16A (rT16A mutant) and rIBV-E-A26F (rA26F mutant). These mutant viruses could be recovered from electroporated Vero cells, and their E gene sequences were verified. The effect of these mutations on IBV production was monitored by analysis of plaque size and growth curves in infected Vero cells. Plaques formed by both IC-inactive mutants were similar in morphology to those caused by wild-type rIBV (WT-rIBV), although they were slightly smaller for the rA26F mutant (Fig. 2A). The growth kinetics of the two mutants was studied with Vero cells infected at a multiplicity of infection (MOI) of ~2, whereby virus titers in both cell lysates and culture supernatants were determined by plaque assay. In these experiments, after lysis by three freeze-thaw cycles, virus titers of cells infected by WT-rIBV and rT16A or rA26F mutants were similar (Fig. 2B); i.e., IBV E IC activity is not essential for virus replication in cell culture. Consistently, levels of IBV positive-sense subgenomic RNA2, or IBV structural proteins, were similar for cells infected with WT-rIBV or IBV E mutants (Fig. 2C and D). However, we note that at a late stage of infection (40 h postinfection [hpi]), the

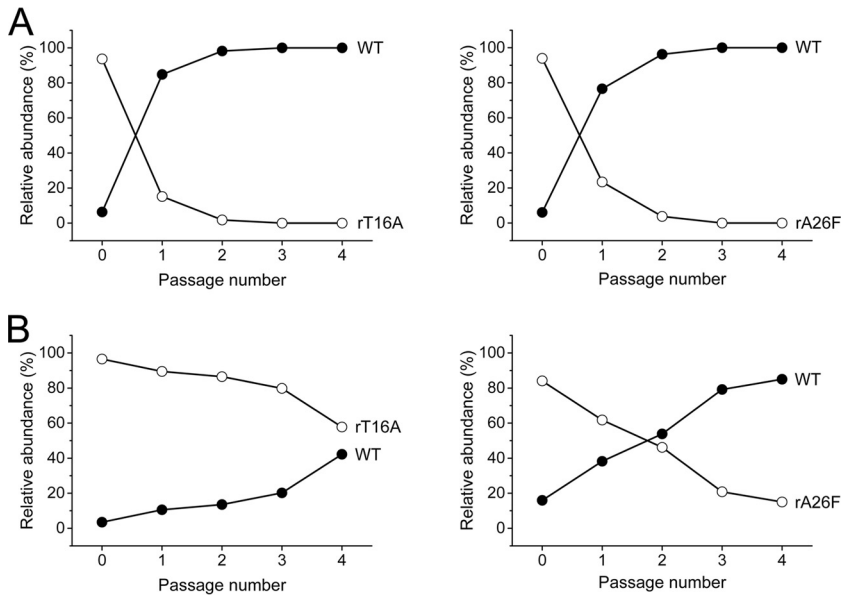

FIG 3 Contribution of IBV E IC activity to viral fitness and virion release. Competition assays between the WT-rIBV (WT; closed circles) and rT16A or rA26F mutant viruses (open circles) were performed in Vero cells coinfected at a wild type/mutant ratio of 1:9. Either the culture supernatant (A) or whole-cell lysates (B) were serially passaged every 24 h four times. The quantification of the relative abundance of each virus was performed by sequencing the IBV E gene within the viral progeny.

amount of the cleaved form of IBV S protein was lower in rT16A mutant-infected cells (not shown), suggesting that the T16A mutation affects S protein trafficking and maturation.

IBV E protein IC activity is required for the efficient release of infectious virions. In contrast to the cell lysate results, the titers of the two mutants at 16, 24, and 32 hpi in the culture supernatant were 1 log lower than those corresponding to the WT virus at the same time points (Fig. 2E). Two explanations may account for this observation: (i) the IC-inactive mutant viruses might be less efficient in releasing mature virions, and (ii) the released mature virions might be less infectious. Thus, the culture supernatant was tested for levels of IBV positive-sense genomic RNA and IBV structural proteins. While S, M, and N proteins were detected in the supernatant of cells infected with the wild-type IBV at 24 hpi, no expression could be detected in cells infected with the mutants (Fig. 2D). Consistently, IBV positive-sense genomic RNA was present at significantly lower levels in the supernatants of cells infected with the rT16A and rA26F mutants compared to WT-rIBV-infected cells (Fig. 2F). These results show that these mutations affect the efficient release of mature virions from infected cells. Since both mutants are IC inactive, this suggests that IBV E protein IC activity may play a crucial role in viral release.

IBV E IC activity improves viral fitness and virion release. To investigate the effect of these mutations on viral fitness, competition assays were performed between the WT and mutants. Vero cells were coinfected with each mutant and WT at a 9:1 ratio. After 24 h, the resulting virus population was serially passaged, either with only the culture supernatant (supernatant passage) or with the total cell lysate (total cell lysate passage). Analysis of the viral population in the culture supernatant of infected Vero cells showed that WT-rIBV rapidly overtook each of the two IBV E mutants at the first passage, while at the same time the quantities of both mutants decreased (Fig. 3A).

When the viral population in the total cell lysate was studied, the substitution took place at a lower rate, but it was also apparent. The rT16A mutant still remained dominant in the population after four passages, but the tendency showed a steady decline in favor of the WT virus (Fig. 3B). In the case of the rA26F mutant, the WT virus outcompeted the mutant after only two passages. These results and those in Fig. 2A

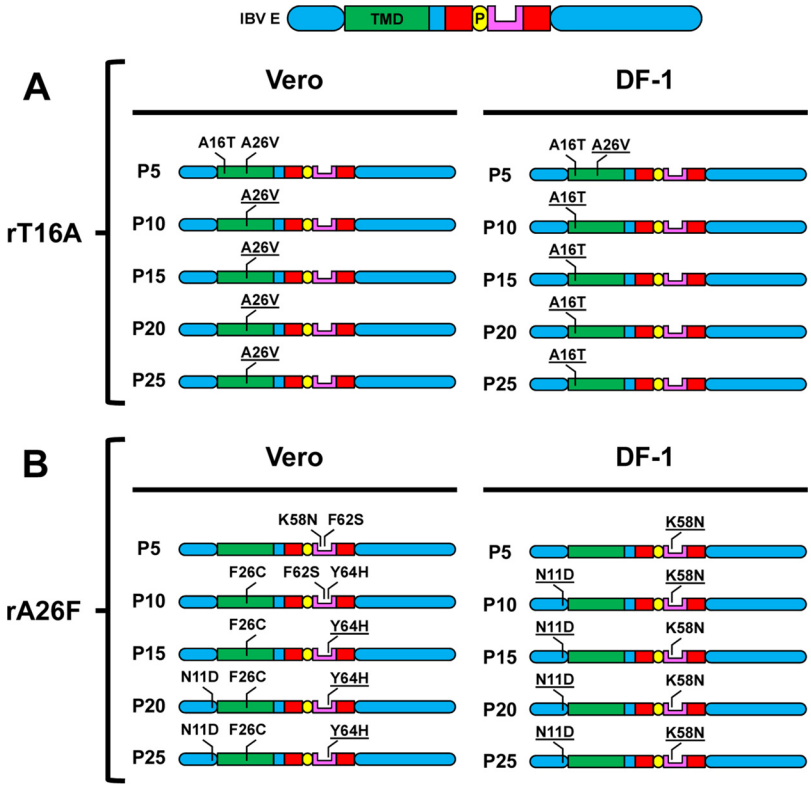

FIG 4 Mutations acquired by IC-inactive mutants after serial passages. Vero and DF-1 cells were infected with the rT16A (A) or rA26F (B) mutant. The mutations observed are indicated in passages P5 to P25, where underlined mutations dominate in population over the wild-type residue at the corresponding positions. Regions of IBV E are indicated by color codes: TMD, green; predicted β-structure, red; flanking conserved Pro55, yellow circle; inserted sequence, pink (see Fig. 1); and remaining EMD, blue.

show that the A26F mutant is more seriously challenged than the T16A mutant. A similar set of competition assays was performed in DF-1 cells, where WT-rIBV outcompeted both IBV mutants in a similar fashion (not shown). These results show that the two mutant viruses were challenged in fitness and release. In both aspects, the WT virus outcompeted the mutants.

rIBV E IC-inactive mutants evolve revertant E mutations. If the effects induced by these mutations are due to the loss of IC activity, serial passage of mutant viruses in cell culture should enable the appearance of compensatory mutations in E protein with recovered IC activity. Thus, WT and mutant viruses were serially passaged 25 times in Vero or DF-1 cells every 24 h, and the E gene was sequenced at passages 0 (P0), 5, 10, 15, 20, and 25 (P25). In Vero cells infected with WT-rIBV, the E gene was stable throughout the passages (not shown). However, in cells infected with the rT16A mutant, the E gene acquired mutation A26V after only 5 passages in both types of cells, but this mutation remained only in Vero cells (Fig. 4A, left).

It is noticeable that although the conversion to the native residue (from Ala to Thr) requires only a single nucleotide change, i.e., a transition (G↔A), Ala in T16A did not revert to Thr in Vero cells even after 25 passages. However, reversion to the original Thr16 residue took place early in DF-1 chicken fibroblast cells (Fig. 4A, right), from P5. The fact that A26V appeared in both Vero and DF-1 cells infected with the rT16A mutant suggests that its acquisition is advantageous for the virus. These results suggest that although the IBV used is adapted to Vero cells, there is not enough pressure to change Thr16 if IBV E has IC activity. However, when this residue is mutated and IC activity is abolished, solutions other than reverting to Thr16 are preferred. In contrast, chickens are the natural hosts of IBV, and DF-1 cells may provide a more biologically relevant selective pressure to regain the native Thr16.

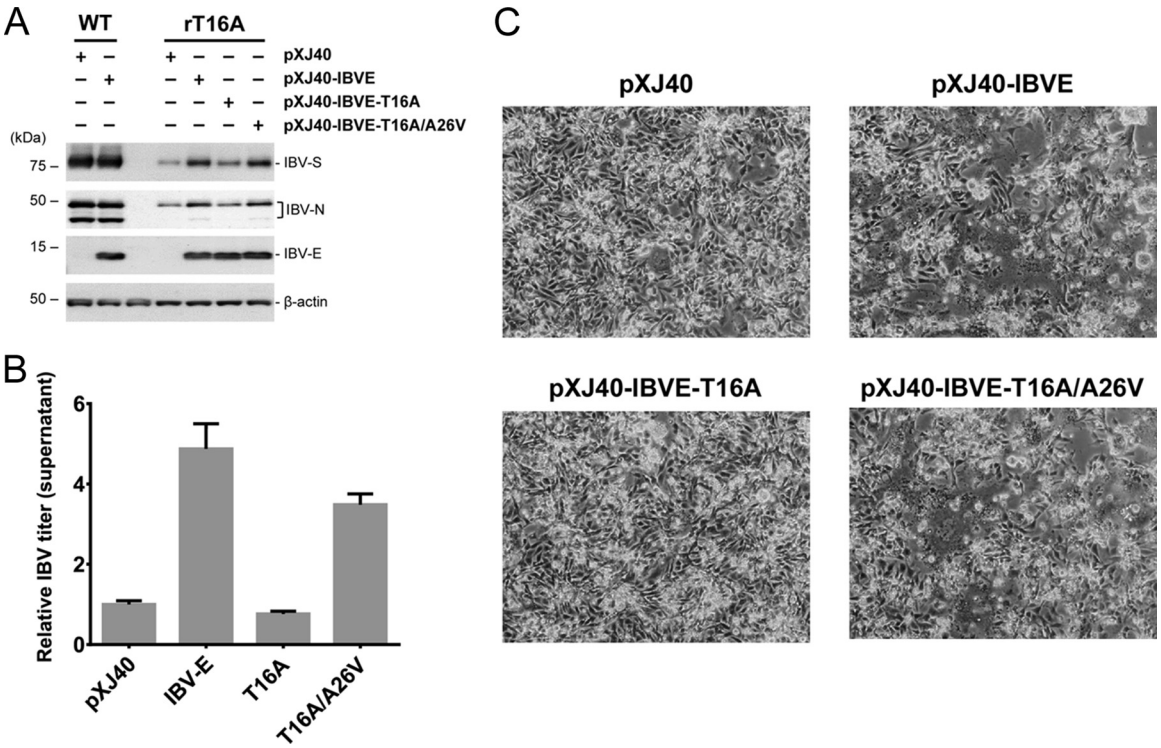

FIG 5 Phenotype recovery of the rT16A mutant after addition of IC-active IBV E (WT or T16A/A26V) in *trans*. DF-1 cells were transfected with the plasmids indicated for 24 h, followed by infection with the rT16A mutant for 24 h. (A) Western blot analysis of whole-cell lysates, with WT-rIBV-infected cells as a control. (B) IBV titer in culture supernatants of rT16A mutant-infected cells determined by plaque assay. The values are relative to the first column (relative IBV titer = 1), found in cells transfected with control vector pXJ40. Error bars represent standard deviations ($n = 3$). (C) Cytopathic effects (CPE) observed under the conditions indicated.

In contrast to the rT16A mutant, the rA26F mutant produced revertants with mutations at extramembrane domains (EMDs) (Fig. 4B). In Vero cells (Fig. 4B, left), the E gene rapidly acquired mutations K58N and F62S in the insert sequence (Fig. 1). In subsequent passages, the insert only contained mutation Y64H, complemented with N11D at the N terminus and F26C in the TMD. When passaging was performed in DF-1 cells, only mutations K58N, which appeared only transiently in Vero cells, and N11D, were observed (Fig. 4B, right).

Defective virion release caused by IC-inactive mutants can be rescued by WT or revertant IBV E introduced in *trans*. It may be possible that the rescue of viral fitness is due to acquired mutations outside the E gene during serial passage of the recombinant IC-inactive IBV. To rule out this possibility, E proteins (WT or a T16A/A26V revertant mutant) were introduced in *trans* to DF-1 cells infected with the rT16A mutant.

In the first case, cells were first transfected with the vector pXJ40 or pXJ40-IBVE, followed by infection with WT-rIBV at an MOI of ~0.05. When cells were transfected with pXJ40-IBVE, a significantly higher level of IBV E was observed than with the pXJ40 vector-transfected cells (Fig. 5A). Similar levels of IBV S and N proteins were detected in the lysates of WT-rIBV-infected cells with or without transfected IBV E, demonstrating that overexpression of IBV E has no effect on the replication of IBV structural proteins in infected cells. In contrast, when cells were infected with the rT16A mutant and transfected with pXJ40-IBVE, significantly higher levels of IBV S and N were observed. Consistently, a roughly 3-fold increase in the supernatant IBV titers was observed in this sample compared to that transfected with the pXJ40 vector control alone (Fig. 5B).

Cells infected with the rT16A mutant and transfected with the pXJ40-IBVE-T16A/A26V revertant mutant also enhanced levels of IBV S and N protein significantly compared to infected cells transfected with pXJ40-IBVE-T16A alone (Fig. 5A). This is consistent with the higher titers of IBV in culture supernatant after addition of IBVE-

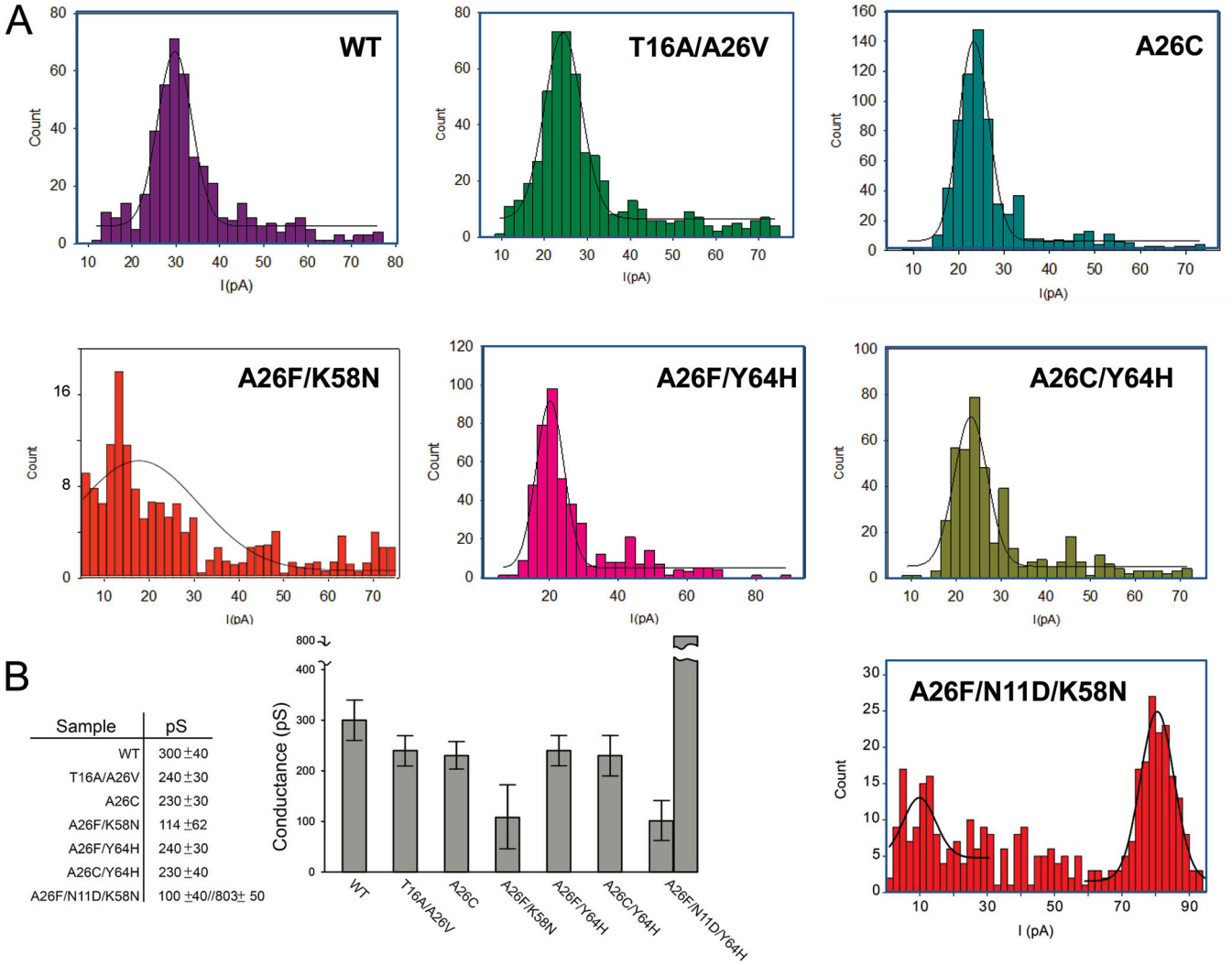

FIG 6 IBV E IC conductance measurements. (A) Histograms corresponding to the intensities detected for purified IBV E protein and mutants incorporated in black lipid membranes (BLM) in 500 mM KCl at pH 6. The membranes contained DOPC:DOPS:DOPE at a 3:1:1 molar ratio. T16A, L25F, A26F, L26F, T16D, and T16N mutants were IC inactive (not shown). (B) Conductance (in pS) of the samples shown in panel A. We note that IBV-E shows similarities with other viroporins regarding lipid involvement in pore formation. This might explain the width of the histogram plots and the fact that some mutants do permeabilize the membrane but that "channels" are short-lived, presumably because of a less efficient stabilization of peptide α-helices by lipids. Highly noisy current traces would be consistent with this view of poor lipid-peptide stabilization that leads to dispersion in conductance values.

T16A/A26V in *trans*. While the transfection of pXJ40-IBVE-T16A failed to recover the cytopathic effect (CPE) of rT16A mutant-infected cells, transfection with pXJ40-IBVE-T16A/A26V resulted in a CPE comparable to that caused by transfection with wild-type IBV E (pXJ40-IBVE) (Fig. 5C). Overall, these experiments demonstrate that the T16A/A26V revertant introduced in *trans* can be used to recover lost fitness in the rT16A virus and that the compensatory mutation A26V made in the E gene of the recombinant IBV was sufficient for this purpose.

Effect of mutations on E protein IC activity. To test if the observed revertant mutations restored the IC activity of the E protein, IBV E proteins carrying these mutations were expressed and purified and studied in a black lipid membrane setup. In most cases, the IC activities of the observed revertant mutants were comparable to that of the WT (Fig. 6). However, in the case of the A26F/K58N and A26F/N11D revertant mutants, the protein appeared to be more difficult to insert in the bilayer. For the A26F/N11D mutant, 4 to 5 times more protein was required to observe a signal. Even then, defined currents were not observed for this mutant; only events of 300 pS or more, which may represent unstable structures or very large pores with conductances

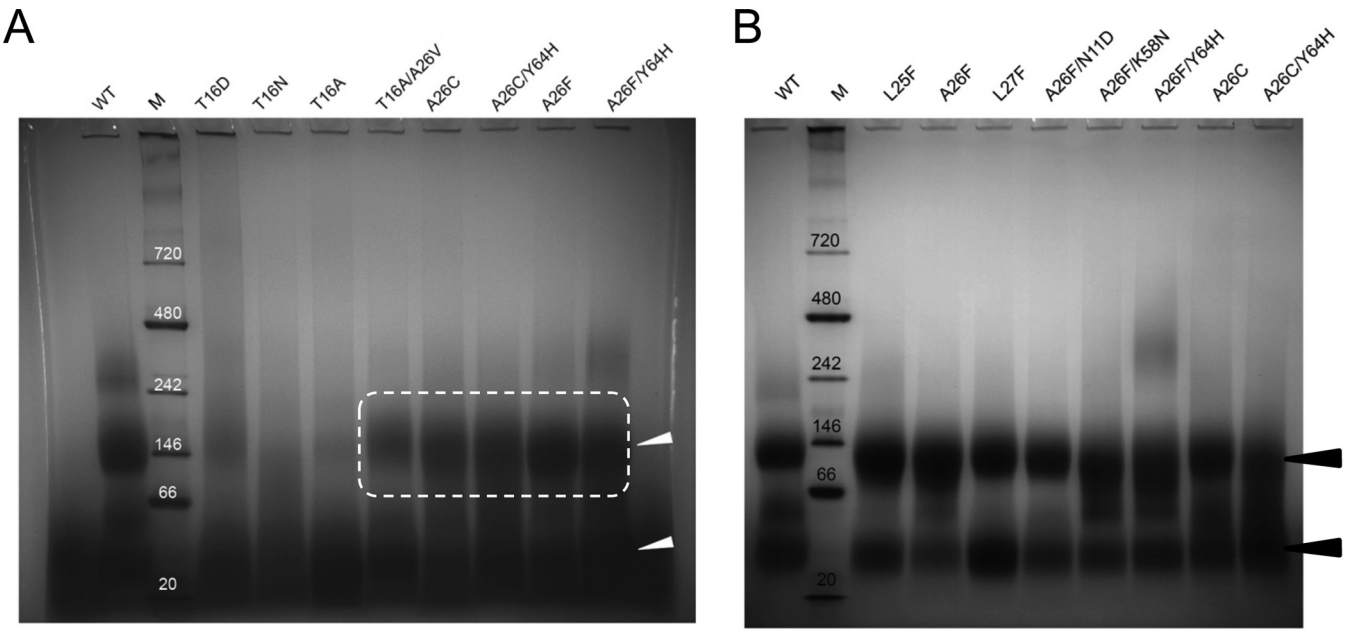

FIG 7 Oligomerization of IBV E and its mutants. Results of BN-PAGE electrophoresis of IBV E WT and mutants are shown. (A) Mutants observed in Vero cells; white arrowheads point to pentamers (upper, dotted box) and monomers (lower); (B) mutants observed in DF-1 cells and L25F and L27F mutants. Gels were run after the sample was solubilized in 20 mM LMPG detergent. Black arrows indicate pentamers and monomers, as in panel A. The same molecular weight markers (M) are used in both panels.

around 4 to 6 nS (not shown). For the A26F/K58N revertant mutant, conductance was about half of that of the other revertant mutants. In this case, defined channels appeared but not frequently, which resulted in a larger error in the measured conductance. The A26F/N11D/K58N triple mutant was better behaved and showed IC activity but with a different pattern with respect to the WT. The histogram shows that there are IC events which differ considerably in conductance: a clear peak at ~800 pS, another small, less defined, peak at ~100 pS, and also IC events with a broad range of conductances between them. The 100-pS events lasted for tens of seconds, whereas the 800-pS events lasted typically only hundreds of milliseconds. Overall, these results clearly suggest that the two compensatory mutations, N11D and K58N, must be present in the same protein to regain IC activity.

To test if other polar residues are able to recover IC activity when substituting for the native IBV E Thr16, two additional E mutants, the T16N and T16D mutants, were also tested for IC activity. Asn is the equivalent polar residue present in the alignment for SARS-CoV E protein (Fig. 1), whereas Asp was acquired by the recombinant rSARS-CoV-E-N15A and regained IC activity (32). Neither of these mutants displayed IC activity (not shown), supporting the hypothesis that the identity of the polar residue at this position 16 is specific for each CoV E protein.

Effect of mutations on E protein oligomerization. Because of its predicted interhelical orientation, the A26F mutation is expected to disrupt E channel oligomerization. However, the above results show that most revertant mutations for the rA26F mutant, except F26C in Vero cells, appeared in EMDs (Fig. 4). This is clearly in contrast with a similar SARS-CoV E mutant, the V25F mutant, which acquired several mutations that clustered along the helix interface opposite Val25 (32). Thus, we tested the effect of these mutations on IBV E oligomerization, using blue-native polyacrylamide gel electrophoresis (BN-PAGE) gels.

Quite unexpectedly, mutation T16A disrupted oligomer formation in BN-PAGE gels (Fig. 7A), and this was also the case for the T16N and T16D mutants, which clearly explains the lack of IC activity in these mutants. Consistently, the IC-active revertant mutant for rT16A, the T16A/A26V mutant, regained the ability to form oligomers. In the same gel, the A26F mutant and its revertant mutants in Vero cells, the A26C, A26F/

Y64H, and A26C/Y64H mutants, retained the ability to form oligomers. This suggests that in this case, the cause of IC inactivation is not the disruption of the IBV E oligomers. The A26F revertant mutants observed in DF-1 cells, the A26F/N11D and A26F/K58N mutants, also preserved a WT-like oligomer (Fig. 7B).

One possible explanation for the preservation of the oligomeric form in the A26F mutant is that A26F in IBV E is not at an interfacial position. However, we also tested the contiguous L25F and L27F mutants, showing that these also preserve native-like oligomerization (Fig. 7B). When tested for IC activity, these two mutants displayed a pattern of behavior similar to that of the A26F mutant, with occasional but very noisy and unstable currents that cannot be ascribed to bona fide ion channels (not shown). Since at least one of these three residues should have an interfacial orientation, it seems likely that insertion of a Phe residue at this interfacial position does not disrupt the IBV E oligomer.

Overall, IC activity and oligomerization results indicate that T16A revertant mutants tend to restabilize the oligomer and at the same time recover IC function. In contrast, the effect of A26F revertant mutants appears to reverse an A26F-induced IC-inactivating conformational change in the IBV E oligomer. Since most of these compensatory mutations appear only at EMDs, this conformational change may be effective either through direct physical contact between the central region of the TMD and EMDs or indirectly through some allosteric mechanism. These alternatives highlight the possibility of a second TMD, as predicted by some algorithms (Fig. 1, TM2), or an embedded hairpin encompassing this region, which is predicted as being more hydrophobic. Unfortunately, no structural data are currently available for IBV E. To test if EMD residues Lys58 and Tyr64 can affect IC activity, they were mutated to Ala and the IBV E mutants were expressed and purified before being tested for IC activity. While the K58A mutant produced few stable IC events, the Y64A mutant produced many IC events that were stable, between 100 to 500 pS. Therefore, a mutation at K58 affects IC activity, whereas Y64A has only a minor effect on IC activity. This is consistent with the way in which revertant mutations appeared: mutation Y64H was present only when mutation F26C appeared, which is already active by itself (although A26F/Y64H seems to have IC activity as well [Fig. 6]). In contrast, K58N produced an active channel even when A26F was still present (Fig. 4B).

Secondary structure of IBV E in SDS and LMPG micelles. Since most of the compensatory mutations acquired by the rA26F mutant appeared in predicted EMDs of IBV E, we tested the possibility that IBV E has more than one TMD or an unexpected topology. Isotopically labeled IBV E was purified (Fig. 8) and reconstituted in detergent micelles for NMR studies. Several detergent systems were tested, and most of them failed to produce acceptable spectra (not shown). Only sodium dodecyl sulfate (SDS) and lyso-myristoylphosphatidylglycerol (LMPG) produced spectra of reasonable quality for structural studies.

Backbone resonance assignment could be achieved for most of the protein. However, despite the use of a perdeuterated sample, resonances corresponding to ~10 residues in the predicted C-terminal EMD were not observed, even in the presence of SDS. To determine whether oligomerization of E protein was responsible for the missing residues, E protein was titrated with increasing SDS and/or diluted. Oligomerization was monitored using BN-PAGE gels. However, even under conditions in which IBV E was 100% monomeric, the spectral quality did not improve (data not shown), suggesting that the region with missing resonances is exposed to an intermediate exchange between two or more conformations.

The secondary structure of IBV E in both SDS and LMPG micelles was predicted based on the chemical shifts by using TALOS+ and showed mostly a succession of α-helical and coil stretches (Fig. 9). In SDS, there are five α-helical stretches, H1 to H5 (Fig. 9A). The N-terminal region down to Ala45 appears almost entirely α-helical but is seemingly interrupted at Gly12 and Ala41. These residues delimit the only TM α-helix (H2), flanked by short α-helices N- and C-terminally (H1 and H3, respectively). At the

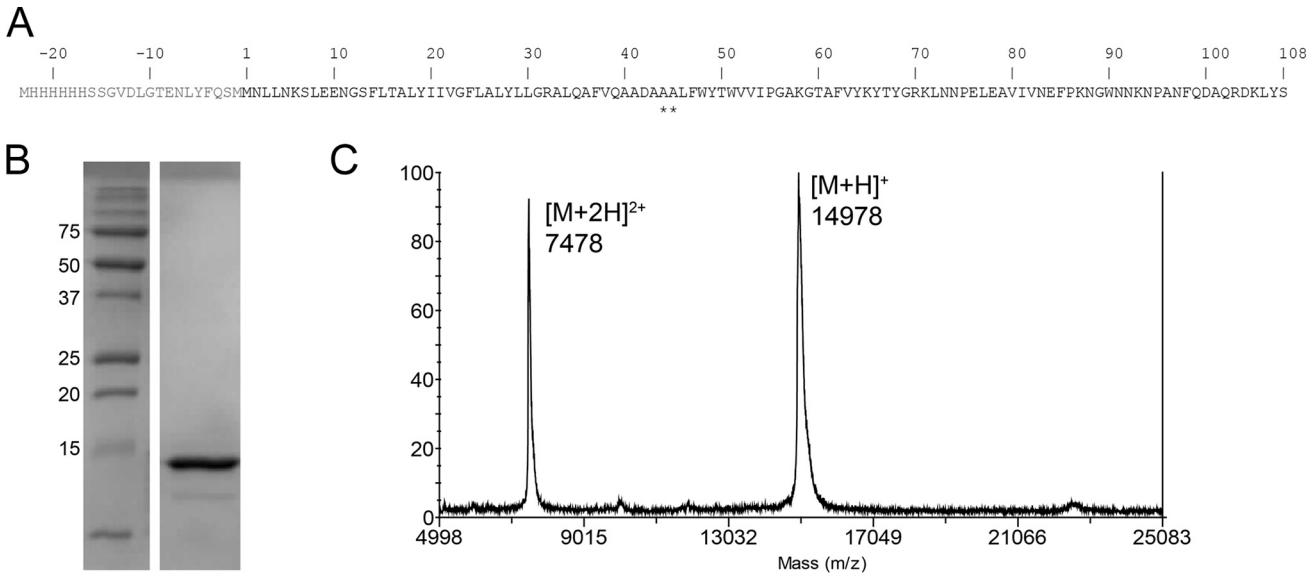

FIG 8 Full-length IBV E protein construct. (A) Amino acid sequence of full-length IBV E construct used in this paper, numbered to exclude the His tag (from residues −23 to 0 [in gray]). The two mutations, C44A and C45A, are indicated. (B and C) SDS-PAGE (B) and MALDI-TOF MS spectra (C) of the HPLC-purified E protein. Expected molecular size is 14,978 Da.

C-terminal end, two additional short α-helices span Gly56 to Gly69 (H4) and Pro75 to Glu84 (H5), respectively. Since some residues within these stretches are resistant to hydrogen-deuterium (H/D) exchange (see below), H4 and H5 are probably bound to the SDS micelle surface. In LMPG (Fig. 9B), the N-terminal α-helical stretch formed by H1 to

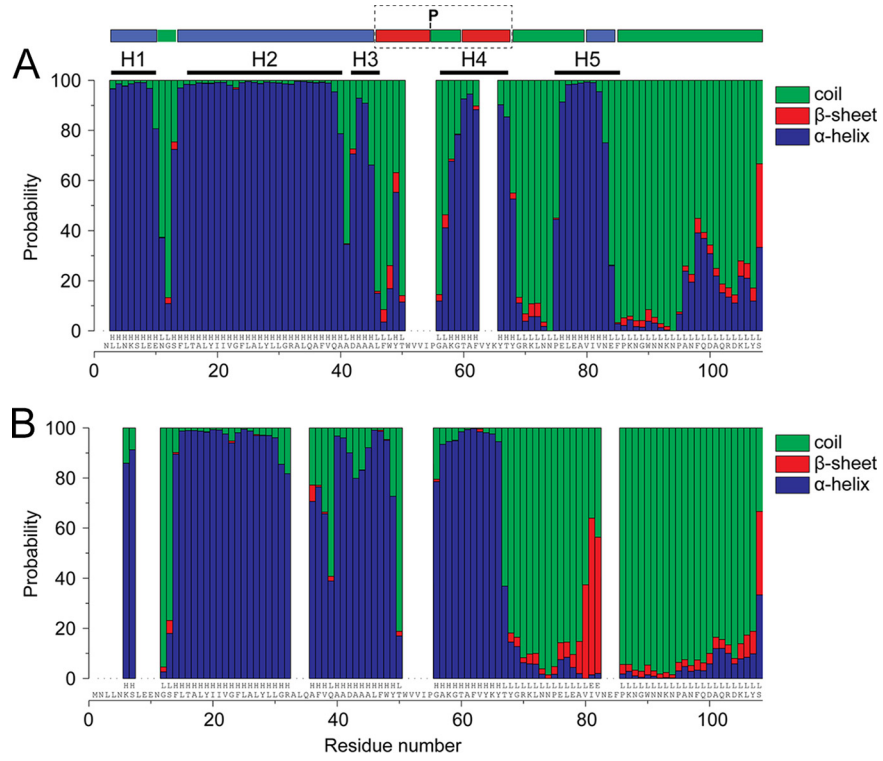

FIG 9 Secondary structure of IBV E. The predicted secondary structure (color coded) of IBV E according to standard prediction tools (72) is shown at the top of the figure. (A and B) TALOS+ chemical shift-based predictions of secondary structure in SDS (A) and LMPG (B), with consensus indicated underneath each vertical bar (H, helix; E, sheet; L, loop). Each vertical bar shows a color-coded distribution of probabilities for the different secondary-structure types.

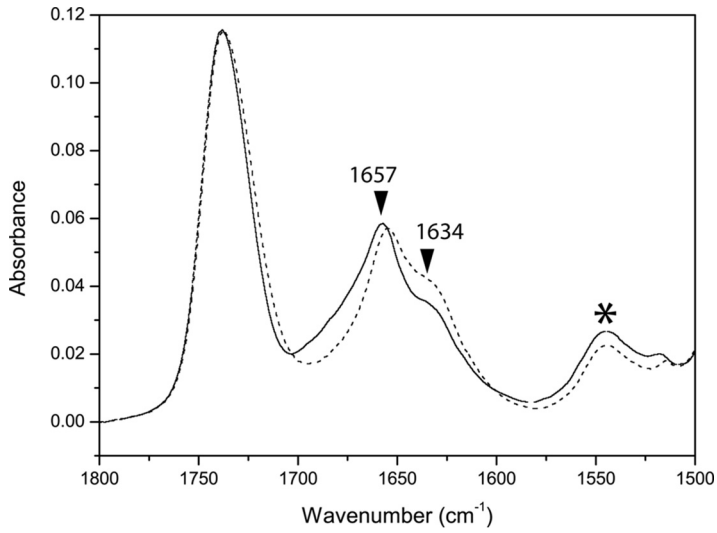

FIG 10 Infrared spectra of IBV E incorporated in DMPC lipid bilayers. Nonpolarized infrared spectra of the amide I and II regions in H_2O at low hydration (solid line) or hydrated in D_2O (broken line) are shown. The amide II is indicated by a star. Arrowheads indicate the maxima in the amide I band. The small reduction in amide II intensity after D_2O exposure is due to N-H to N-D conversion.

H3 extends until Thr50. This is followed by a helical stretch analogous to H4 in SDS but slightly shorter, from Gly56 to Thr67. H5 is not observed in LMPG and may be unfolded or may partially adopt β-structure.

Consistent with the data obtained with detergents, IBV E incorporated in DMPC lipid bilayers (Fig. 10) has an amide I band centered at 1,657 cm^{-1}, typical of α-helix. This shows that the secondary structure of IBV E in lipid bilayers is predominantly α-helical, although the contribution of random coil is possible but difficult to evaluate. Additionally, a small but clear shoulder represents β-structure, at ~1,634 cm^{-1}. This β-structure may correspond to the predicted β-structure regions in IBV E around Pro55 (Fig. 9, top) and may be favored in a lipidic environment.

Membrane-embedded regions of IBV E in SDS and DMPC lipid bilayers. Although LMPG produced good NMR spectra, in this detergent only 4 to 5 resonances were found to be resistant to H/D exchange in a ^{1}H-^{15}N TROSY-HSQC (transverse relaxation optimized spectroscopy-heteronuclear single quantum coherence spectroscopy) experiment (not shown). However, in SDS, 26 residues in the first predicted TMD region were found to be resistant to exchange, from Asn11 to Ala36 (Fig. 11A). This represents a single TMD, although slightly longer than the predicted one (Fig. 1, TM1). Other parts of IBV E are also partially protected from H/D exchange, e.g., juxtamembrane residues Ala41 and Ala44, as well as residues in the C-terminal EMD, e.g., Tyr66, Gly69, Asn73, Leu77, and Ile81 (Fig. 11B). This last region may correspond to an α-helix tightly bound to the detergent surface. Overall, the H/D exchange data obtained in SDS is not compatible with the presence of a second TMD or membrane-embedded hairpin in the C-terminal EMD. Under these conditions, physical contact between Ala26 and the "insert" sequence K^{58}GTAFV seems unlikely.

However, incorporation of IBV E in DMPC lipid bilayers shows that after exposure to D_2O, only 20 to 30% of the amide II band is reduced (Fig. 10). This represents between 76 and 87 residues protected from exchange and, in principle, is compatible with a second TMD or an embedded hairpin in the C-terminal EMD.

DISCUSSION

Effect on virion release. Our results show that the rIBV E IC-inactive T16A and A26F mutants display kinetics in genome replication/transcription, protein translation, and virus assembly inside the infected cells similar to those of the wild-type virus but lead to a reduction in the release of infectious virions. It is known that CoV virions appear

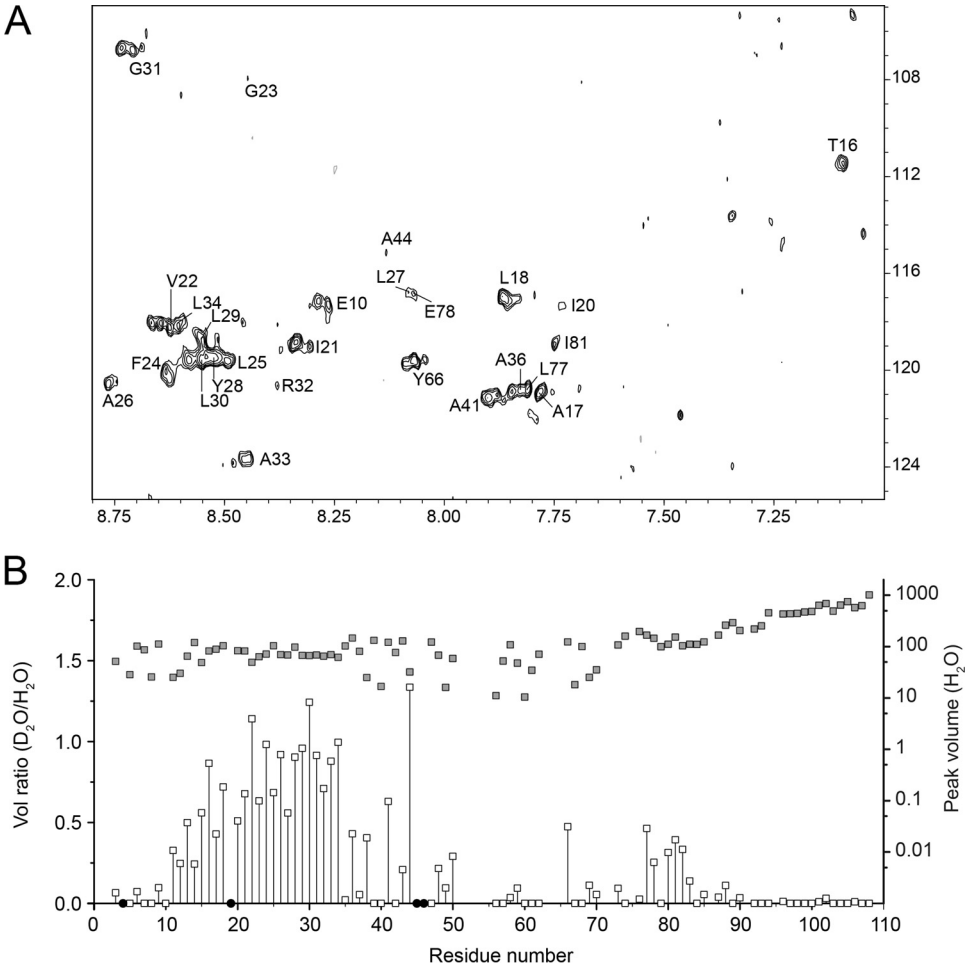

FIG 11 H/D exchange of IBV E in SDS. (A) ^{1}H-^{15}N TROSY-HSQC spectrum of IBV E in SDS, in the presence of 99% D_2O, with H/D exchange-resistant cross-peaks indicated; (B) protection from H/D exchange expressed as a volume ratio of D_2O/H_2O peaks (open squares). Residues that cannot be measured due to overlap are excluded (filled circles). Peak volumes in H_2O are plotted in a logarithmic scale (filled squares), i.e., larger volumes produce more reliable values.

in large vacuoles derived from Golgi complex/ERGIC membranes (41) and that CoV infections are characterized by rearrangements of host cell membranes (40); these alterations and efficient trafficking of virions are facilitated by IBV E (38–42). Thus, the reduced virion release for these IC-inactive mutants suggests a role for E protein IC activity in efficient shedding of mature virions. Previous reports have shown that substitution of a nonoligomerizing TMD for the IBV E TMD led to the intracellular accumulation of viral particles (38), highlighting the importance of the IBV E TMD for the forward trafficking of cargo to the plasma membrane through the Golgi complex. Incidentally, our preliminary studies suggest that the mutations introduced here also resulted in differential activation of cellular response pathways, such as alterations in the induction of apoptotic cell death and production of proinflammatory cytokines (not shown).

Here, we have shown that, as with SARS-CoV (32), IBV E revertant mutants bearing the T16A and A26F mutations restored both IC activity and viral fitness. However, the patterns of revertant mutations observed in the two cases are very different.

IBV E A26F mutation. At variance with the results obtained for the SARS-CoV E V25F mutation, most compensatory changes elicited by IBV E A26F were not located at the TMD but at the N-terminal (N11D) or C-terminal (K58N, F62S, and Y64H) EMDs. In the C-terminal EMDs, the changes clustered to an insert region unique to gamma-CoV, K^{58}GTAFV (Fig. 1). This is surprising, since mutation A26F, like SARS E V25F, is expected

to disrupt TM-TM interactions. However, neither A26F, L25F, nor L27F was particularly disrupting to IBV E oligomerization in BN-PAGE gels. The interpretation that A26F is not monomeric is further reinforced by the revertant mutants obtained herein, since changes occur mostly in EMD regions. Therefore, these results suggest that the observed revertant mutations do not act to recover oligomerization but to adjust the existing oligomer conformation. It is also possible that apart from its effect on IC activity, the A26F mutation may have had other unidentified adverse effects on IBV during the course of infection.

The rA26F compensatory mutations observed differed slightly depending on the cell type used for the passage. For example, although most compensatory mutations clustered along the unique insert sequence of the IBV E protein, mutation Y64H appeared only when the virus was passaged in Vero cells. However, these small differences may not be reproducible. It also remains to be tested whether these compensatory mutations, especially those found in Vero cells, can lead to a recovery of native phenotype when introduced in the chicken embryo system.

We hypothesize that the differences observed in SARS-CoV and IBV E revertant mutants are related to the presence of the insert in the C-terminal EMD of IBV E. It is possible that Ala26 and residues in the insert that appeared to be mutated in response to A26F, i.e., K58N, F62S, and Y64H, are in physical contact through a second TMD or an embedded hairpin in the C-terminal EMD. Although only one TMD was observed in SDS micelles, H/D exchange protection in DMPC membranes is as high as 70 to 80%. Therefore, since cellular membranes are the native environment for IBV E, it is likely that most of the protein is embedded in, or tightly bound to, the membrane.

Although the present data cannot exclude the possibility of a second TMD in cellular membranes, this is unlikely because SARS-CoV E and MERS E have similar high percentages (~70%) of H/D exchange-protected residues when analyzed by infrared (IR) spectroscopy in model lipid bilayers, yet SARS-CoV E has a $N_{exo}C_{cyto}$ topology (24) consistent with a single TMD, and both SARS-CoV E and MERS E have a single predicted TMD confirmed by H/D exchange experiments in detergent micelles (45, 46). Likewise, there is an overwhelming evidence of a $N_{exo}C_{cyto}$ topology for IBV E (39, 43, 48), which implies the presence of only one TMD.

The possibility that the membrane environment, but not SDS micelles, facilitates formation of an embedded hairpin or loop, or more tightly bound α-helices, seems more likely. This would allow direct regulation of the TMD through modifications in the insert region of IBV E. Alternatively, these changes may just affect monomer-monomer and/or monomer-membrane interactions at the EMD through helices H1 (N11D) and H4 (Fig. 1, insert region) and allosterically alter the TMD, reinstating in the oligomer some lost flexibility that is necessary for IC activity.

IBV E T16A mutation. Similarly to the N15A mutation in SARS-CoV E (32), in the present work, the IBV E mutation T16A did not mutate to other polar residues at this position. It can be argued that this is because mutation of Ala16 to polar residues other than Thr would involve at least two nucleotide changes in the codon. However, neither of the possible E protein mutants we tested, i.e., the T16D or T16N mutant, recovered the oligomeric form in BN-PAGE gels or IC activity. This again supports that this polar residue is specific for each CoV E sequence. This could be related to their different effects on E protein oligomerization: in SARS-CoV E, the N15A mutant formed more stable oligomers than the V25F mutant (49), while in contrast, in IBV E, the T16A mutant destabilized the oligomer, while its revertant mutants recovered both the ability to oligomerize and the IC activity. Also, we found that the T16A mutant and those with similar polar residues at that position are monomeric but that T16A revertant mutants also recover the ability to oligomerize.

A recent study based on the analysis of IBV E in transfected cells reaches opposite conclusions regarding the oligomeric state of the T16A and A26F mutants (50). The latter study analyzed nonquantitatively the relative sedimentation of IBV E in a sucrose gradient after extraction from transfected cells with the detergent DDM (*n*-dodecyl-β-

D-maltoside). In these experiments, WT IBV E appeared in two fractions assigned to low (monomeric)- and high (oligomeric)-molecular-weight pools at an approximately 40:60 ratio. When cells were transfected with the A26F and T16A mutants, only one fraction appeared: low (A26F) or high (T16A). Consistent with previous results (38, 39), the same paper (50) showed that T16A, but not A26F, prevented Golgi complex disassembly and reduced the trafficking of vesicular stomatitis virus (VSV) G but greatly enhanced virus-like particle (VLP) production. The authors associated the effects on Golgi compartment disassembly and trafficking with an IBV E monomeric form present in both the WT and the A26F mutant. VLP production may be related to an oligomeric form (more stable in the T16A mutant), although in previous experiments by the same group, VLP formation did not differ between the WT and the T16A mutant (38, 39). However, we note that when infected cells were used (50), almost all (~95%) of WT IBV E appeared in the high-molecular-weight band. It would be interesting to obtain the above results in infected cells.

While our data are in agreement with the notion that disruptive effects on the secretory pathway and VLP formation and assembly are not related to IC activity, the role of the monomeric and oligomeric forms of IBV E is precisely the opposite: disruption of the secretory pathway is associated with an oligomeric form (WT and A26F mutant), whereas a monomeric form (T16A mutant) enhances VLP formation.

Structural model of IBV E and nonobserved resonances. Despite the prediction of short stretches of β-structure in C-terminal tails of CoV E proteins, no obvious β-structure was detected for IBV E in SDS or LMPG micelles. Instead, the structure appears to be formed by several α-helical stretches, reminiscent of other viroporins (51–53). Residues Val63 to Lys65 were not observable in SDS, but considering that residues immediately flanking this stretch are α-helical, the remaining three residues are likely to be part of an α-helix in H4. This is supported by the α-helical conformation of H4 that could be observed in its entirety in LMPG.

We have suggested previously that the region near the conserved Pro residue in CoV E proteins (Pro55 in IBV E) has a high abundance of β-branched and bulky residues that can potentially destabilize α-helical conformation (45), and this region is predicted to have β-structure (Fig. 9). SARS-CoV E in lipid bilayers has an infrared amide I signature that corresponds to a mostly α-helical protein (45). However, its synthetic fragment 46-60 adopts 100% β-structure (44, 51), and peptides inspired on that domain form amyloid fibers (51, 54), whereas peptide 50-65 forms 100% α-helix (unpublished result). That the region around the conserved Pro55 has structural flexibility is supported by the fact that mutations designed to increase its α-helical propensity produced an IR spectrum with slightly less β-structure and more α-structure (45). Similarly to SARS-CoV E, we have shown that the IR spectrum of IBV E in lipid bilayers is mostly α-helical but shows a minor contribution of β-structure.

For IBV E in detergent, short stretches before and after the conserved Pro55, predicted to form β-structure, were difficult to detect by NMR, even when using a perdeuterated sample. For example, the sequence from Trp51 to Ile54 could not be assigned in SDS or LMPG, and therefore the conformation of this region remains uncertain. This again points to a conformational exchange that takes place at an intermediate rate between α-helix and β-sheet forms. The α-helix form would be more favored in detergent (45), thus broadening the linewidth and preventing the observation of some cross-peaks in this region.

This dynamic exchange may be related to possible roles of E proteins in inducing membrane curvature or in the scission of viral particles from cellular membranes (15, 38, 55–58). Compensatory changes that helped regain virulence were observed in the region around conserved Pro55 after deletion of a C-terminal PDZ-binding motif (PBM) (28, 59) in SARS-CoV E (27), which seems plausible if the region possesses sufficient α-helical propensity. Truncations in the same region of SARS-CoV E also resulted in attenuation (60). This has led to the development of SARS-CoV LAVs based on E-deleted and E-truncated virions (57, 58, 60, 61). Thus, both channel activity and cytoplasmic tail

integrity (60) are required simultaneously to achieve virulence. The native function of this region in SARS-CoV E, as well as H4-H5 helices in IBV E, is unknown, but this region is probably involved in protein-protein interactions.

Vaccines. Based on the locations of the compensatory mutations found in the E protein of rT16A and rA26F mutants, consistent with the results obtained in SARS-CoV E, the rT16A mutant seems to have fewer options that lead to a channel-active mutant, and the mutation even reverted back to the original Thr when serially passaged in DF-1 cells. However, it is possible that the stability of these mutations *in ovo* or *in vivo* may be different from that *in vitro*.

The results point to compensatory mutations for the rA26F mutant located in an insert region characteristic of gamma-CoV. Therefore, a strategy for vaccine development that prevents back-mutations might be to combine the A26F mutation with simultaneous mutations or deletions in this insert region. In addition, given the importance and specificity of the position occupied by a polar residue, Thr16 in IBV E, one may replace this residue with another one that requires two or three transversions. One challenge to overcome in the recovery of LAV produced *in vitro*, however, is that these mutations may render the recombinant virus deficient in virion release, as shown for the rT16A and rA26F mutants, which may compromise the efficient production and purification of the vaccine products.

Overall, the present study establishes the initial basis for such LAV development targeting the IBV E protein and characterizing hot spots that compensate for loss of virulence in IC-inactive mutants.

The results obtained herein are especially relevant for the development of live attenuated IBV vaccines, which, along with inactivated boost vaccines, is one of the promising ways to control IBV infection. Specifically, it would be desirable to directly and rationally engineer mutations with an attenuation of pathogenicity that is difficult to reverse, while at the same time retaining as much immunogenicity as in the wild-type virus. Indeed, currently commercial LAVs are produced after multiple passages of virulent field isolates in embryonated domestic fowl eggs. This has several drawbacks, such as lack of cross-protection due to many different IBV serotypes, reduced viral immunogenicity, mutations that enable back-mutations that recover virulence, and persistent high infectivity and virulence for embryos, which prevents administration *in ovo*.

MATERIALS AND METHODS

Cells and virus. The African green monkey kidney-derived Vero cells and the DF-1 (ATCC CRL-12203) chicken fibroblast cells were obtained from the American Type Culture Collection (ATCC). They were cultured at 37°C in Dulbecco's modified Eagle medium (DMEM) supplemented with 10% fetal bovine serum (FBS), penicillin (100 U/ml), and streptomycin (100 μg/ml). The egg-adapted Beaudette strain of IBV (ATCC VR-22) was obtained from the ATCC and adapted to Vero cells as described previously, i.e., 65 passages on Vero cells (p65) (62). Propagation of IBV was performed in Vero cells in FBS-free DMEM. To prepare virus stock, the cell lysate obtained 24 hpi was treated with three freeze-thaw cycles, followed by clarification at 1,500 $\times$ *g* for 30 min at 4°C, and the supernatant was stored at −80°C. The titer of the virus stock was determined by plaque assays.

Construction of rIBV. Recombinant IBV (rIBV) viruses carrying mutations in the E gene which abolished the IC activity were constructed. Briefly, five fragments spanning the entire IBV genome, fragments A to E, had been previously cloned into pKT0, pCR-XL-TOPO (Invitrogen), or pGEM-T Easy (Promega) vector, flanked by restriction site BsmBI (fragment A) or BsaI (fragments B, C, D, and E) (63). The pGEM construct containing the cDNA fragment (fragment E) spanning the genomic region of nucleotides 20901 to 27608 of IBV, which includes the E gene, was used as the background to introduce mutations using site-directed mutagenesis. Each E fragment contained different point mutations within the E gene that would result in amino acid substitutions to abolish IC activity: T16A (ACA to GCA) and A26F (GCA to TTT). The wild-type fragments A, B, C, and D, as well as the E fragments carrying mutations in the E gene, were digested from the respective plasmids and gel purified. The genomic fragments were assembled by DNA ligation using T4 DNA ligase to generate full-length cDNA clones. *In vitro* transcription was performed using the mMessage mMachine T7 kit (Ambion, Austin, TX), according to the manufacturer's instructions. In addition, an N transcript was generated using the IBV N gene and the 3′ untranslated region (UTR) as the templates. The IBV full-length and N transcripts were purified with phenol-chloroform before introduction into Vero cells by electroporation. The rIBVs were harvested from the cell supernatant, and the engineered mutations in the E gene were validated by real-time PCR (RT-PCR) and DNA sequencing as described below.

RNA extraction and RT-PCR analysis. Total RNA from cultured cells was extracted with TRIzol reagent (Invitrogen) according to the manufacturer's instructions. Briefly, cells were lysed with 1 ml TRIzol per 10 cm^2 effective growth area, and the lysates were mixed with one-fifth volume of chloroform. After centrifugation at 12,000 × *g* at 4°C for 15 min, the aqueous phase was mixed with an equal volume of isopropanol. RNA was pelleted by centrifugation at 12,000 × *g* at 4°C for 15 min, washed twice with 70% ethanol, and reconstituted in RNase-free water. The cDNA was reverse transcribed from total RNA using the oligo(dT) primer and ImProm-II reverse transcription system (Promega) according to the manufacturer's instructions. Real-time PCR was performed using a SYBR select PCR kit (Life Technologies) in an Applied Biosystems 7500 real-time PCR system (Applied Biosystems) according to the manufacturer's instructions. The following PCR primers (forward and reverse) were used: IBV subgenomic RNA2, 5′-CTATTATACTAGCCTTGCGCTAGA-3′ and 5′-AGGTGTTACCAACATCTCTCACC-3′; IBV total RNA, 5′-AGTAGCTTGGAAACGAACGGT-3′ and 5′-CGGCACTGGCATCTTTAGAC-3′; β-actin, 5′-TACGCCAACACAGTGCTGTCT-3′ and 5′-TCTGCATCCTGTCGGCAAT-3′.

Virus genome sequencing. The IBV genome region spanning nucleotides 23944 to 24693 that contains the E gene was sequenced after reverse transcription and PCRs. Briefly, total RNA from infected cells was extracted as described above. To obtain the cDNA, 5 μg of extracted RNA was reverse transcribed using the oligo(dT) primer. The cDNA product was used as the template for the subsequent PCR using forward primer 5′-CGCTCCAACAACTAATACAAG-3′, reverse primer 5′-AATGTTAAGGGGCCAAAAGC-3′, and the Q5 DNA polymerase (New England BioLabs), in accordance with the manufacturer's instructions. The PCR product was purified using the Wizard DNA Clean-Up system (Promega) and sequenced with primer 5′-TTGAAACTGGTGAGCAAGTGA-3′.

Growth kinetics and plaque assays. Culture supernatants of IBV-infected cells collected at different time points were clarified by centrifugation, followed by 10-fold serial dilution using serum-free DMEM. The viral titers were determined by plaque assay. Briefly, diluted supernatants were applied to confluent monolayers of Vero cells. After 2 h of adsorption, medium was removed and cells were washed twice with DMEM. Cells were overlaid with DMEM containing 0.4% agarose and incubated at 37°C for 2 days. The agarose overlay was removed, and cells were fixed with 4% formaldehyde before staining with crystal violet. Finally, the plaque numbers were counted, and the titers of individual samples were expressed in the unit of logarithm of PFU per ml. Each sample was titrated in triplicate in each experiment.

Genetic stability through serial passaging of rIBVs lacking IC activity. Confluent monolayers of Vero or DF-1 cells cultured in 35-mm^2 dishes were infected with WT-rIBV, rIBV-E-T16A (rT16A), or rIBV-E-A26F (rA26F) at an MOI of 2. At 24 hpi, culture supernatants were collected and passaged on fresh monolayers of cells. The rIBVs were serially passaged 25 times, in which the E gene was sequenced at passages 0, 5, 10, 15, 20, and 25 as described above.

Virus competition assays. Vero and DF-1 cells were used for competition assays. Cells were coinfected with WT-rIBV and mutant rIBVs at a ratio of 1:9. The viral population was studied in two ways. In one set of experiments, culture supernatants were collected at 24 hpi and passaged on a fresh monolayer of cells. In another set of experiments, cells were washed twice at 24 hpi and subjected to three freeze-thaw cycles and the cell lysates were used to infect subsequent passages of cells. The viruses were serially passaged four times in both sets. Total RNA from the coinfected cells was isolated, and the IBV E gene was sequenced as described above. The relative abundance of the WT-rIBV and mutant rIBVs was determined as previously described (32).

Plasmids and transfection. The cDNA sequence of IBV E was amplified by RT-PCR of RNA extracted from IBV-infected cells by using primers 5′-CGGAATTCCACCATGAATTTATTGAATAAG-3′ and 5′-CCGCTCGAGTCAAGAGTACAATTTGTC-3′. The PCR product was inserted into vector pXJ40 using EcoRI and XhoI restriction sites. Mutations of the IBV E protein which abolish its IC activity were generated by site-directed mutagenesis using the following primers: T16A Forward, 5′-CGCTAGAGGAGAATGGAAGTTTTCTAGCAGCGCTTTACATA-3′, and T16A Reverse, 5′-TATGTAAAGCGCTGCTAGAAAACTTCCATTCTCCTCTAGCG-3′; A26F Forward, 5′-CAGCGCTTTACATAATTGTAGGATTTTTATTTCTTTATCTTCTAGGTAGAGCACTTCAAG-3′, and A26F Reverse, 5′-CTTGAAGTGCTCTACCTAGAAGATAAAGAAATAAAAATCCTACAATTATGTAAAGCGCTG-3′. Transfection was performed using Lipofectamine 2000 reagent (Invitrogen) according to the manufacturer's instructions. Briefly, cells were plated in 12-well plates and transfected with 0.8 μg of plasmid DNA. At 24 h posttransfection, cells were infected with IBV at MOI of 0.05 and continued to be incubated before being harvested for protein and/or RNA for analysis.

Western blot analysis. Harvested cells were centrifuged at 16,000 × *g* for 1 min, and the cell pellets were lysed in 1× radioimmunoprecipitation assay (RIPA) buffer. Cell lysates were analyzed by Western blotting using the appropriate antibodies. The antisera against IBV S, E, M, and N proteins were obtained from rabbits immunized with bacterially expressed fusion proteins as previously described (64, 65). β-Actin acted as a loading control. Bound primary antibodies were detected using anti-mouse or anti-rabbit IgG antibodies conjugated with horseradish peroxidase (Dako) and with a chemiluminescence detection kit (Amersham Biosciences) in accordance with the manufacturer's instructions. All experiments were repeated at least three times, with similar results, and one of the representative results is shown.

Protein expression and purification. Both IC activity and NMR results were obtained using full-length IBV E with an N-terminal 6×His tag, followed by a tobacco etch virus cleavage sequence. The two native cysteine residues (Cys44 and Cys45) were mutated to alanine in all constructs to improve the yield and purity of the expressed protein. IBV E forms pentamers in perfluoro-octanoic acid (PFO) gels, whether as native form or as a Cys-less C44A/C45A mutant (44). The IVB E gene was cloned into pNIC28-Bsa4. Mutations in IBV E were introduced by site-directed mutagenesis. The constructs were transformed into *Escherichia coli* strain BL21(DE3) CodonPlus for protein expression. Cells cultured

overnight at 37°C in LB broth was diluted 1:100 into fresh Terrific Broth medium and allowed to grow until an optical density at 600 nm (OD_{600}) reached 2. Protein expression was induced by the addition of 0.5 mM isopropyl β-D-1-thiogalactopyranoside (IPTG). After an overnight culture at 18°C, cells were harvested by centrifugation at 7,500 × g.

Stable isotope-labeled E protein for NMR was produced by initially growing an *E. coli* culture in LB medium at 37°C to an OD_{600} of 0.7. The cell mass was then transferred to M9 minimal medium at 4 times the concentration factor as described previously (66). The M9 medium was appropriately supplemented with [^{15}N]NH_4Cl, [^{13}C]glucose/[^{13}CD]glucose, and D_2O (Cambridge Isotope Laboratories) to produce ^{15}N-, ^{15}N/^{13}C-, or ^{15}N/^{13}C/D-labeled protein. Protein expression was induced by adding 0.5 mM IPTG. After further culture at 18°C for 6 h, the cells were harvested by centrifugation at 7,500 × *g*.

Cell pellets were resuspended in lysis buffer containing 20 mM Tris-HCl (pH 8.0), 300 mM NaCl, 5 mM imidazole, 2 mM β-mercaptoethanol (β-ME), and 10% glycerol, supplemented with 1 mM phenylmethylsulfonyl fluoride (PMSF) and 0.1% lauryldimethylamine N-oxide (LDAO). Cell lysis was achieved by brief sonication, followed by passing the cells through a microfluidizer (Microfluidics, USA) five times at 10×10^3 to 12×10^3 lb/in^2. Insoluble particles were removed by centrifugation at 40,000 × *g* for 30 min at 4°C, and the supernatant was loaded onto a nickel-nitrilotriacetic acid resin (Bio-Rad Profinity IMAC, Ni^{2+} charged) preequilibrated with lysis buffer. After overnight binding at 4°C, the resin was washed with 20 mM Tris-HCl (pH 8.0), 300 mM NaCl, 20 mM imidazole, 2 mM β-ME, and 10% glycerol. IBV E protein was eluted with 20 mM Tris-HCl (pH 8.0), 300 mM NaCl, 250 mM imidazole, 2 mM β-ME, 10% glycerol, and 0.1% LDAO. The eluent was precipitated with trichloroacetic acid (TCA), lyophilized, and further purified by reversed-phase high-performance liquid chromatography (HPLC) by applying a linear gradient of an isopropanol-acetonitrile (IPA-ACN) mixture (80:20 [vol/vol] with 0.1% TFA) on a Phenomenex Jupiter C_4 column (250 by 10 mm, 300-Å pore size, 5-μm particle size). The identity and purity of peptide fractions were confirmed by SDS-PAGE and in-gel trypsin digestion, followed by matrix-assisted laser desorption ionization–time of flight tandem mass spectrometry (MALDI-TOF MS-MS).

Conductance measurements. The experiments reported here were carried out in single ion channels reconstituted on planar membranes. Planar bilayer membranes were formed from two monolayers prepared from a lipid mixture containing 1,2-dioleoyl-*sn*-glycero-3-phosphocholine (DOPC), 1,2-dioleoyl-sn-glycero-3-phospho-L-serine (DOPS), and 1,2-dioleoyl-*sn*-glycero-3-phosphoethanolamine (DOPE) at a 3:1:1 (DOPC:DOPS:DOPE) ratio in pentane on 70- to 90-μm-diameter orifices in the 15-μm-thick Teflon partition that separates two identical chambers (67, 68). The orifices were pretreated with a 1% solution of hexadecane in pentane. Aqueous solutions of KCl were buffered with 5 mM HEPES at pH 6. All measurements were performed at room temperature. Single-channel insertion was achieved by adding 2 to 3 μl of a 150-μg/ml solution of protein in the buffer that contains acetonitrile-isopropanol (40:60) on the *cis* side of the chamber.

An electric potential was applied using Ag/AgCl electrodes in 2 M KCl–1.5% agarose bridges assembled within standard 250-ml pipette tips. The potential was defined as positive when it was higher on the side of the protein addition (the *cis* side of the membrane chamber), whereas the *trans* side was set to ground. An Axopatch 200B amplifier (Molecular Devices, Sunnyvale, CA) in the voltage clamp mode was used to measure the current and applied potential. The chamber and the head stage were isolated from external noise sources with a double metal screen (Amuneal Manufacturing Corp., Philadelphia, PA). The single-channel conductance was obtained from the current measurement at an applied potential of +100 mV in symmetrical salt solutions.

Gel electrophoresis. Blue-native PAGE (BN-PAGE) was performed as described previously (69). Lyophilized peptide was solubilized at 0.1 mM in sample buffer containing 20 mM lyso-myristoylphosphatidylglycerol (LMPG).

NMR spectroscopy. Lyophilized IBV E protein was solubilized at 0.8 mM in 50 mM sodium phosphate (pH 5.5), 50 mM NaCl, and 200 mM SDS or LMPG. For H/D exchange experiments, solubilized IBV E sample was relyophilized overnight and resolubilized in D_2O. NMR experiments were performed at 313 K with Avance-II 700 NMR spectrometers with cryogenic probes. Sodium 2,2-dimethyl-2-silapentane-5-sulfonate (DSS) was used as the internal reference for ^{1}H nuclei. The chemical shifts of ^{13}C and ^{15}N nuclei were indirectly referenced from the ^{1}H chemical shifts (http://www.bmrb.wisc.edu/ref_info/cshift.html). NMR data were processed using Bruker TopSpin 3.1 and analyzed using CARA (http://cara.nmr.ch/). Sequence-specific assignment of backbone $^1H^N$, ^{15}N, $^{13}C'$, $^{13}C^\alpha$, and $^{13}C^\beta$ was achieved by using 2D [^{1}H-^{15}N]-TROSY-HSQC, 3D HNCO, HN(CA)CO, HNCA, HN(CO)CA, HNCACB, and CBCA(CO)NH on a ^{15}N/^{13}C/D-labeled IBV E protein. Secondary structure was predicted using TALOS+ (70).

Infrared spectroscopy. IBV E incorporation in DMPC lipid bilayers and collection of ATR-FTIR (attenuated total reflection-Fourier transform infrared) spectra was performed as described previously (34). Approximately 100 μl of sample with a 50:1 lipid/protein molar ratio was applied to a trapezoidal (50 mm × 2 mm × 20 mm) Ge internal reflection element (IRE). The areas of the amide I (C = O stretching) and amide II (N-H bending, centered at ~1,550 cm^{-1}) were obtained by peak integration from 1,600 to 1,700 cm^{-1} and from 1,510 cm^{-1} to 1,580 cm^{-1}. The hydrogen-deuterium (H/D) exchange was calculated by measuring the relative area of the amide II to amide I band, before and after addition of D_2O, as described previously (34).

ACKNOWLEDGMENTS

We thank T. Cornvik, A. Oi, and E. K. M. Nilsson from the NTU/SBS Protein Production Platform for the expression screening of IBV E protein constructs.

REFERENCES

1. Beaudette FR, Hudson CB. 1937. Cultivation of the virus of infectious bronchitis. J Am Vet Med Assoc 90:51–60.
2. Sjaak de Wit JJ, Cook JKA, van der Heijden HMJF. 2011. Infectious bronchitis virus variants: a review of the history, current situation and control measures. Avian Pathol 40:223–235. https://doi.org/10.1080/03079457.2011.566260.
3. McMartin DA. 1993 Infectious bronchitis, p 249–274. *In* McFerran JB, McNulty MS (ed), Virus infections of birds. Elsevier Science Publishers, Amsterdam, the Netherlands.
4. Enjuanes L, Brian D, Cavanagh D, Holmes K, Lai MMC, Laude H, Masters P, Rottier P, Siddell SG, Spaan WJM, Taguchi F, Talbot P. 2000. Coronaviridae, p 835–849. *In* van Regenmortel MHV, Fauquet CM, Bishop DHL, Carsten EB, Estes MK, Lemon SM, McGeoch DJ, Maniloff J, Mayo MA, Pringle CR, Wickner RB (ed), Virus taxonomy: classification and nomenclature of viruses: seventh report of the International Committee on Taxonomy of Viruses. Academic Press, San Diego, CA.
5. Woo PCY, Lau SKP, Huang Y, Yuen KY. 2009. Coronavirus diversity, phylogeny and interspecies jumping. Exp Biol Med 234:1117–1127. https://doi.org/10.3181/0903-MR-94.
6. de Groot RJ, Cowley JA, Enjuanes L, Faaberg KS, Perlman S, Rottier PJM, Snijder EJ, Ziebuhr J, Gorbalenya AE. 2011. Coronaviridae. International Union of Microbiological Societies VDEAP, London, United Kingdom.
7. Holmes KV. 2003. SARS coronavirus: a new challenge for prevention and therapy. J Clin Invest 111:1605–1609. https://doi.org/10.1172/JCI18819.
8. Raj VS, Osterhaus ADME, Fouchier RAM, Haagmans BL. 2014. MERS: emergence of a novel human coronavirus. Curr Opin Virol 5:58–62. https://doi.org/10.1016/j.coviro.2014.01.010.
9. Lou Z, Sun Y, Rao Z. 2014. Current progress in antiviral strategies. Trends Pharmacol Sci 35:86–102. https://doi.org/10.1016/j.tips.2013.11.006.
10. Kilianski A, Baker SC. 2014. Cell-based antiviral screening against coronaviruses: developing virus-specific and broad-spectrum inhibitors. Antiviral Res 101:105–112. https://doi.org/10.1016/j.antiviral.2013.11.004.
11. Kilianski A, Mielech AM, Deng X, Baker SC. 2013. Assessing activity and inhibition of Middle East respiratory syndrome coronavirus papain-like and 3C-like proteases using luciferase-based biosensors. J Virol 87:11955–11962. https://doi.org/10.1128/JVI.02105-13.
12. Wei YQ, Guo HC, Dong H, Wang HM, Xu J, Sun DH, Fang SG, Cai XP, Liu DX, Sun SQ. 2014. Development and characterization of a recombinant infectious bronchitis virus expressing the ectodomain region of S1 gene of H120 strain. Appl Microbiol Biotechnol 98:1727–1735. https://doi.org/10.1007/s00253-013-5352-5.
13. Lv L, Li X, Liu G, Li R, Liu Q, Shen H, Wang W, Xue C, Cao Y. 2014. Production and immunogenicity of chimeric virus-like particles containing the spike glycoprotein of infectious bronchitis virus. J Vet Sci 15:209–216. https://doi.org/10.4142/jvs.2014.15.2.209.
14. Graham RL, Becker MM, Eckerle LD, Bolles M, Denison MR, Baric RS. 2012. A live, impaired-fidelity coronavirus vaccine protects in an aged, immunocompromised mouse model of lethal disease. Nat Med 18:1820–1826. https://doi.org/10.1038/nm.2972.
15. Enjuanes L, Nieto-Torres JL, Jimenez-Guardeno JM, DeDiego ML. 2011. Recombinant live vaccines to protect against the severe acute respiratory syndrome coronavirus, p 73–97. *In* Dormitzer PR, Mandt C, Rappuoli R (ed), Replicating vaccines: a new generation. BAID—Birkhäuser Advances in Infectious Diseases. Springer, Basel, Switzerland.
16. Jackwood MW. 2012. Review of infectious bronchitis virus around the world. Avian Dis 56:634–641. https://doi.org/10.1637/10227-043012-Review.1.
17. Heald-Sargent T, Gallagher T. 2012. Ready, set, fuse! The coronavirus spike protein and acquisition of fusion competence. Viruses 4:557–580. https://doi.org/10.3390/v4040557.
18. Masters PS. 2006. The molecular biology of coronaviruses. Adv Virus Res 66:193–292. https://doi.org/10.1016/S0065-3527(06)66005-3.
19. Liao Y, Yuan Q, Torres J, Tam JP, Liu DX. 2006. Biochemical and functional characterization of the membrane association and membrane permeabilizing activity of the severe acute respiratory syndrome coronavirus envelope protein. Virology 349:264–275. https://doi.org/10.1016/j.virol.2006.01.028.
20. Tung FYT, Abraham S, Sethna M, Hung S-L, Sethna P, Hogue BG, Brian DA. 1992. The 9-kDa hydrophobic protein encoded at the 3′ end of the porcine transmissible gastroenteritis coronavirus genome is membrane-associated. Virology 186:676–683. https://doi.org/10.1016/0042-6822(92)90034-M.
21. Corse E, Machamer CE. 2003. The cytoplasmic tails of infectious bronchitis virus E and M proteins mediate their interaction. Virology 312:25–34. https://doi.org/10.1016/S0042-6822(03)00175-2.
22. Raamsman MJB, Krijnse Locker J, De Hooge A, De Vries AAF, Griffiths G, Vennema H, Rottier PJM. 2000. Characterization of the coronavirus mouse hepatitis virus strain A59 small membrane protein E. J Virol 74:2333–2342. https://doi.org/10.1128/JVI.74.5.2333-2342.2000.
23. Lopez LA, Riffle AJ, Pike SL, Gardner D, Hogue BG. 2008. Importance of conserved cysteine residues in the coronavirus envelope protein. J Virol 82:3000–3010. https://doi.org/10.1128/JVI.01914-07.
24. Nieto-Torres JL, DeDiego ML, Alvarez E, Jimenez-Guardeno JM, Regla-Nava JA, Llorente M, Kremer L, Shuo S, Enjuanes L. 2011. Subcellular location and topology of severe acute respiratory syndrome coronavirus envelope protein. Virology 415:69–82. https://doi.org/10.1016/j.virol.2011.03.029.
25. DeDiego ML, Nieto-Torres JL, Regla-Nava JA, Jimenez-Guardeño JM, Fernandez-Delgado R, Fett C, Castaño-Rodriguez C, Perlman S, Enjuanes L. 2014. Inhibition of NF-κB-mediated inflammation in severe acute respiratory syndrome coronavirus-infected mice increases survival. J Virol 88:913–924. https://doi.org/10.1128/JVI.02576-13.
26. DeDiego ML, Nieto-Torres JL, Jimenez-Guardeno JM, Regla-Nava JA, Alvarez E, Oliveros JC, Zhao J, Fett C, Perlman S, Enjuanes L. 2011. Severe acute respiratory syndrome coronavirus envelope protein regulates cell stress response and apoptosis. PLoS Pathog 7:e1002315. https://doi.org/10.1371/journal.ppat.1002315.
27. Jimenez-Guardeno JM, Regla-Nava JA, Nieto-Torres JL, DeDiego ML, Castano-Rodriguez C, Fernandez-Delgado R, Perlman S, Enjuanes L. 2015. Identification of the mechanisms causing reversion to virulence in an attenuated SARS-CoV for the design of a genetically stable vaccine. PLoS Pathog 11:e1005215. https://doi.org/10.1371/journal.ppat.1005215.
28. Jimenez-Guardeno JM, Nieto-Torres JL, DeDiego ML, Regla-Nava JA, Fernandez-Delgado R, Castano-Rodriguez C, Enjuanes L. 2014. The PDZ-binding motif of severe acute respiratory syndrome coronavirus envelope protein is a determinant of viral pathogenesis. PLoS Pathog 10:e1004320. https://doi.org/10.1371/journal.ppat.1004320.
29. Verdia-Baguena C, Nieto-Torres JL, Alcaraz A, DeDiego ML, Torres J, Aguilella VM, Enjuanes L. 2012. Coronavirus E protein forms ion channels with functionally and structurally-involved membrane lipids. Virology 432:485–494. https://doi.org/10.1016/j.virol.2012.07.005.
30. Wilson L, Gage P, Ewart G. 2006. Hexamethylene amiloride blocks E protein ion channels and inhibits coronavirus replication. Virology 353:294–306. https://doi.org/10.1016/j.virol.2006.05.028.
31. Torres J, Maheswari U, Parthasarathy K, Ng LF, Liu DX, Gong XD. 2007. Conductance and amantadine binding of a pore formed by a lysine-flanked transmembrane domain of SARS coronavirus envelope protein. Protein Sci 16:2065–2071. https://doi.org/10.1110/ps.062730007.
32. Nieto-Torres JL, DeDiego ML, Verdia-Baguena C, Jimenez-Guardeno JM, Regla-Nava JA, Fernandez-Delgado R, Castano-Rodriguez C, Alcaraz A, Torres J, Aguilella VM, Enjuanes L. 2014. Severe acute respiratory syndrome coronavirus envelope protein ion channel activity promotes virus fitness and pathogenesis. PLoS Pathog 10:e1004077. https://doi.org/10.1371/journal.ppat.1004077.
33. Parthasarathy K, Ng L, Lin X, Liu DX, Pervushin K, Gong X, Torres J. 2008. Structural flexibility of the pentameric SARS coronavirus envelope protein ion channel. Biophys J 95:L39–41. https://doi.org/10.1529/biophysj.108.133041.
34. Torres J, Parthasarathy K, Lin X, Saravanan R, Kukol A, Ding XL. 2006. Model of a putative pore: the pentameric α-helical bundle of SARS coronavirus E protein in lipid bilayers. Biophys J 91:938–947. https://doi.org/10.1529/biophysj.105.080119.
35. Pervushin K, Tan E, Parthasarathy K, Xin L, Jiang FL, Yu D, Vararattanavech A, Soong TW, Liu DX, Torres J. 2009. Structure and inhibition of the SARS coronavirus envelope protein ion channel. PLoS Pathog 5:e1000511. https://doi.org/10.1371/journal.ppat.1000511.
36. Torres J, Wang J, Parthasarathy K, Liu DX. 2005. The transmembrane oligomers of coronavirus protein E. Biophys J 88:1283–1290. https://doi.org/10.1529/biophysj.104.051730.
37. Acevedo A, Brodsky L, Andino R. 2014. Mutational and fitness landscapes of an RNA virus revealed through population sequencing. Nature 505:686–690. https://doi.org/10.1038/nature12861.
38. Ruch TR, Machamer CE. 2011. The hydrophobic domain of infectious bronchitis virus E protein alters the host secretory pathway and is important for release of infectious virus. J Virol 85:675–685. https://doi.org/10.1128/JVI.01570-10.

39. Ruch TR, Machamer CE. 2012. A single polar residue and distinct membrane topologies impact the function of the infectious bronchitis coronavirus E protein. PLoS Pathog 8:e1002674. https://doi.org/10.1371/journal.ppat.1002674.
40. Lavi E, Wang Q, Weiss SR, Gonatas NK. 1996. Syncytia formation induced by coronavirus infection is associated with fragmentation and rearrangement of the Golgi apparatus. Virology 221:325–334. https://doi.org/10.1006/viro.1996.0382.
41. Ulasli M, Verheije MH, de Haan CAM, Reggiori F. 2010. Qualitative and quantitative ultrastructural analysis of the membrane rearrangements induced by coronavirus. Cell Microbiol 12:844–861. https://doi.org/10.1111/j.1462-5822.2010.01437.x.
42. Ruch TR, Machamer CE. 2012. The coronavirus E protein: assembly and beyond. Viruses 4:363–382. https://doi.org/10.3390/v4030363.
43. Corse E, Machamer CE. 2000. Infectious bronchitis virus E protein is targeted to the Golgi complex and directs release of virus-like particles. J Virol 74:4319–4326. https://doi.org/10.1128/JVI.74.9.4319-4326.2000.
44. Parthasarathy K, Lu H, Surya W, Vararattanavech A, Pervushin K, Torres A. 2012. Expression and purification of coronavirus envelope proteins using a modified beta-barrel construct. Protein Expr Purif 85:133–141. https://doi.org/10.1016/j.pep.2012.07.005.
45. Li Y, Surya W, Claudine S, Torres J. 2014. Structure of a conserved Golgi complex-targeting signal in coronavirus envelope proteins. J Biol Chem 289:12535–12549. https://doi.org/10.1074/jbc.M114.560094.
46. Surya W, Li Y, Verdià-Bàguena C, Aguilella VM, Torres J. 2015. MERS coronavirus envelope protein has a single transmembrane domain that forms pentameric ion channels. Virus Res 201:61–66. https://doi.org/10.1016/j.virusres.2015.02.023.
47. Kall L, Krogh A, Sonnhammer EL. 2007. Advantages of combined transmembrane topology and signal peptide prediction—the Phobius web server. Nucleic Acids Res 35:W429–432. https://doi.org/10.1093/nar/gkm256.
48. Yuan Q, Liao Y, Torres J, Tam JP, Liu DX. 2006. Biochemical evidence for the presence of mixed membrane topologies of the severe acute respiratory syndrome coronavirus envelope protein expressed in mammalian cells. FEBS Lett 580:3192–3200. https://doi.org/10.1016/j.febslet.2006.04.076.
49. Torres J, Surya W, Li Y, Liu DX. 2015. Protein-protein interactions of viroporins in coronaviruses and paramyxoviruses: new targets for antivirals? Viruses 7:2858–2883. https://doi.org/10.3390/v7062750.
50. Westerbeck JW, Machamer CE. 2015. A coronavirus E protein is present in two distinct pools with different effects on assembly and the secretory pathway. J Virol 89:9313–9323. https://doi.org/10.1128/JVI.01237-15.
51. Surya W, Samsó M, Torres J. 2013. Structural and functional aspects of viroporins in human respiratory viruses: respiratory syncytial virus and coronaviruses, p 47–76. *In* Vats M (ed), Respiratory disease and infection—a new insight. InTech, Rijeka, Croatia. https://doi.org/10.5772/53957.
52. To J, Surya W, Torres J. 2016. Targeting the ion channel activity of viroporins. *In* Donev R (ed), Advances in protein chemistry and structural biology: ion channels as therapeutic targets, part B, vol 104. Elsevier, Amsterdam, Netherlands.
53. OuYang B, Xie S, Berardi MJ, Zhao X, Dev J, Yu W, Sun B, Chou JJ. 2013. Unusual architecture of the p7 channel from hepatitis C virus. Nature 498:521–525. https://doi.org/10.1038/nature12283.
54. Ghosh A, Pithadia AS, Bhat J, Bera S, Midya A, Fierke CA, Ramamoorthy A, Bhunia A. 2015. Self-assembly of a nine-residue amyloid-forming peptide fragment of SARS corona virus E-protein: mechanism of self aggregation and amyloid-inhibition of hIAPP. Biochemistry 54:2249–2261. https://doi.org/10.1021/acs.biochem.5b00061.
55. Fischer F, Stegen CF, Masters PS, Samsonoff WA. 1998. Analysis of constructed E gene mutants of mouse hepatitis virus confirms a pivotal role for E protein in coronavirus assembly. J Virol 72:7885–7894.
56. Corse E, Machamer CE. 2002. The cytoplasmic tail of infectious bronchitis virus E protein directs Golgi targeting. J Virol 76:1273–1284. https://doi.org/10.1128/JVI.76.3.1273-1284.2002.
57. Netland J, DeDiego ML, Zhao J, Fett C, Alvarez E, Nieto-Torres JL, Enjuanes L, Perlman S. 2010. Immunization with an attenuated severe acute respiratory syndrome coronavirus deleted in E protein protects against lethal respiratory disease. Virology 399:120–128. https://doi.org/10.1016/j.virol.2010.01.004.
58. Lamirande EW, Dediego ML, Roberts A, Jackson JP, Alvarez E, Sheahan T, Shieh WJ, Zaki SR, Baric R, Enjuanes L, Subbarao K. 2008. A live attenuated SARS coronavirus is immunogenic and efficacious in golden Syrian hamsters. J Virol 82:7721–7724. https://doi.org/10.1128/JVI.00304-08.
59. Teoh KT, Siu YL, Chan WL, Schluter MA, Liu CJ, Peiris JS, Bruzzone R, Margolis B, Nal B. 2010. The SARS coronavirus E protein interacts with PALS1 and alters tight junction formation and epithelial morphogenesis. Mol Biol Cell 21:3838–3852. https://doi.org/10.1091/mbc.E10-04-0338.
60. Regla-Nava JA, Nieto-Torres JL, Jimenez-Guardeño JM, Fernandez-Delgado R, Fett C, Castaño-Rodríguez C, Perlman S, Enjuanes L, DeDiego ML. 2015. Severe acute respiratory syndrome coronaviruses with mutations in the E protein are attenuated and promising vaccine candidates. J Virol 89:3870–3887. https://doi.org/10.1128/JVI.03566-14.
61. Almazán F, DeDiego ML, Sola I, Zuñiga S, Nieto-Torres JL, Marquez-Jurado S, Andrés G, Enjuanes L. 2013. Engineering a replication-competent, propagation-defective Middle East respiratory syndrome coronavirus as a vaccine candidate. mBio 4:e00650-13. https://doi.org/10.1128/mBio.00650-13.
62. Ng LFP, Liu DX. 1998. Identification of a 24-kDa polypeptide processed from the coronavirus infectious bronchitis virus 1a polyprotein by the 3C-like proteinase and determination of its cleavage sites. Virology 243:388–395. https://doi.org/10.1006/viro.1998.9058.
63. Fang S, Chen B, Tay FPL, Ng BS, Liu DX. 2007. An arginine-to-proline mutation in a domain with undefined functions within the helicase protein (Nsp13) is lethal to the coronavirus infectious bronchitis virus in cultured cells. Virology 358:136–147. https://doi.org/10.1016/j.virol.2006.08.020.
64. Liu DX, Inglis SC. 1991. Association of the infectious bronchitis virus 3c protein with the virion envelope. Virology 185:911–917. https://doi.org/10.1016/0042-6822(91)90572-S.
65. Li Q, Xiao H, Tam JP, Liu DX. 2006. Sumoylation of the nucleocapsid protein of severe acute respiratory syndrome coronavirus by interaction with Ubc9. Adv Exp Med Biol 581:121–126. https://doi.org/10.1007/978-0-387-33012-9_21.
66. Marley J, Lu M, Bracken C. 2001. A method for efficient isotopic labeling of recombinant proteins. J Biomol NMR 20:71–75. https://doi.org/10.1023/A:1011254402785.
67. Bezrukov SM, Vodyanoy I. 1993. Probing alamethicin channels with water-soluble polymers—effect on conductance of channel states. Biophys J 64:16–25. https://doi.org/10.1016/S0006-3495(93)81336-5.
68. Montal M, Mueller P. 1972. Formation of bimolecular membranes from lipid monolayers and a study of their electrical properties. Proc Natl Acad of Sci U S A 69:3561–3566. https://doi.org/10.1073/pnas.69.12.3561.
69. Gan SW, Vararattanavech A, Nordin N, Eshaghi S, Torres J. 2011. A cost-effective method for simultaneous homo-oligomeric size determination and monodispersity conditions for membrane proteins. Anal Biochem 416:100–106. https://doi.org/10.1016/j.ab.2011.05.007.
70. Shen Y, Delaglio F, Cornilescu G, Bax A. 2009. TALOS+: a hybrid method for predicting protein backbone torsion angles from NMR chemical shifts. J Biomolecular NMR 44:213–223. https://doi.org/10.1007/s10858-009-9333-z.
71. Krogh A, Larsson B, von Heijne G, Sonnhammer EL. 2001. Predicting transmembrane protein topology with a hidden Markov model: application to complete genomes. J Mol Biol 305:567–580. https://doi.org/10.1006/jmbi.2000.4315.
72. Combet C, Blanchet C, Geourjon C, Deleage G. 2000. NPS@: network protein sequence analysis. Trends Biochem Sci 25:147–150. https://doi.org/10.1016/S0968-0004(99)01540-6.